Temperature structure in the Perseus cluster core observed with Hitomi*

Hitomi Collaboration, Felix AHARONIAN,[1,2,3] Hiroki AKAMATSU,[4]
Fumie AKIMOTO,[5] Steven W. ALLEN,[6,7,8] Lorella ANGELINI,[9] Marc AUDARD,[10]
Hisamitsu AWAKI,[11] Magnus AXELSSON,[12] Aya BAMBA,[13,14]
Marshall W. BAUTZ,[15] Roger BLANDFORD,[6,7,8] Laura W. BRENNEMAN,[16]
Gregory V. BROWN,[17] Esra BULBUL,[15] Edward M. CACKETT,[18]
Maria CHERNYAKOVA,[1] Meng P. CHIAO,[9] Paolo S. COPPI,[19,20] Elisa COSTANTINI,[4]
Jelle DE PLAA,[4] Cor P. DE VRIES,[4] Jan-Willem DEN HERDER,[4] Chris DONE,[21]
Tadayasu DOTANI,[22] Ken EBISAWA,[22] Megan E. ECKART,[9] Teruaki ENOTO,[23,24]
Yuichiro EZOE,[25] Andrew C. FABIAN,[26] Carlo FERRIGNO,[10] Adam R. FOSTER,[16]
Ryuichi FUJIMOTO,[27] Yasushi FUKAZAWA,[28] Maki FURUKAWA,[29]
Akihiro FURUZAWA,[30] Massimiliano GALEAZZI,[31] Luigi C. GALLO,[32]
Poshak GANDHI,[33] Margherita GIUSTINI,[4] Andrea GOLDWURM,[34,35] Liyi GU,[4]
Matteo GUAINAZZI,[36] Yoshito HABA,[37] Kouichi HAGINO,[38] Kenji HAMAGUCHI,[9,39]
Ilana M. HARRUS,[9,39] Isamu HATSUKADE,[40] Katsuhiro HAYASHI,[22,41]
Takayuki HAYASHI,[41] Kiyoshi HAYASHIDA,[42] Junko S. HIRAGA,[43]
Ann HORNSCHEMEIER,[9] Akio HOSHINO,[44] John P. HUGHES,[45] Yuto ICHINOHE,[25]
Ryo IIZUKA,[22] Hajime INOUE,[46] Yoshiyuki INOUE,[22] Manabu ISHIDA,[22]
Kumi ISHIKAWA,[22] Yoshitaka ISHISAKI,[25] Masachika IWAI,[22] Jelle KAASTRA,[4,47]
Tim KALLMAN,[9] Tsuneyoshi KAMAE,[13] Jun KATAOKA,[48] Yuichi KATO,[13]
Satoru KATSUDA,[49] Nobuyuki KAWAI,[50] Richard L. KELLEY,[9]
Caroline A. KILBOURNE,[9] Takao KITAGUCHI,[28] Shunji KITAMOTO,[44]
Tetsu KITAYAMA,[51] Takayoshi KOHMURA,[38] Motohide KOKUBUN,[22]
Katsuji KOYAMA,[52] Shu KOYAMA,[22] Peter KRETSCHMAR,[53] Hans A. KRIMM,[54,55]
Aya KUBOTA,[56] Hideyo KUNIEDA,[41] Philippe LAURENT,[34,35] Shiu-Hang LEE,[23]
Maurice A. LEUTENEGGER,[9] Olivier LIMOUSIN,[35] Michael LOEWENSTEIN,[9,57]
Knox S. LONG,[58] David LUMB,[36] Greg MADEJSKI,[6] Yoshitomo MAEDA,[22]
Daniel MAIER,[34,35] Kazuo MAKISHIMA,[59] Maxim MARKEVITCH,[9]
Hironori MATSUMOTO,[42] Kyoko MATSUSHITA,[29] Dan McCAMMON,[60]
Brian R. McNAMARA,[61] Missagh MEHDIPOUR,[4] Eric D. MILLER,[15]
Jon M. MILLER,[62] Shin MINESHIGE,[23] Kazuhisa MITSUDA,[22]
Ikuyuki MITSUISHI,[41] Takuya MIYAZAWA,[63] Tsunefumi MIZUNO,[28,64]
Hideyuki MORI,[9] Koji MORI,[40] Koji MUKAI,[9,39] Hiroshi MURAKAMI,[65]
Richard F. MUSHOTZKY,[57] Takao NAKAGAWA,[22] Hiroshi NAKAJIMA,[42]
Takeshi NAKAMORI,[66] Shinya NAKASHIMA,[59,†] Kazuhiro NAKAZAWA,[13,14]
Kumiko K. NOBUKAWA,[67] Masayoshi NOBUKAWA,[68] Hirofumi NODA,[69,70]

Hirokazu ODAKA**,[6] Takaya O**HASHI**,[25] Masanori O**HNO**,[28] Takashi O**KAJIMA**,[9]
Naomi O**TA**,[67] Masanobu O**ZAKI**,[22] Frits P**AERELS**,[71] Stéphane P**ALTANI**,[10]
Robert P**ETRE**,[9] Ciro P**INTO**,[26] Frederick S. P**ORTER**,[9] Katja P**OTTSCHMIDT**,[9,39]
Christopher S. R**EYNOLDS**,[57] Samar S**AFI-HARB**,[72] Shinya S**AITO**,[44]
Kazuhiro S**AKAI**,[9] Toru S**ASAKI**,[29] Goro S**ATO**,[22] Kosuke S**ATO**,[29] Rie S**ATO**,[22]
Makoto S**AWADA**,[73] Norbert S**CHARTEL**,[53] Peter J. S**ERLEMTSOS**,[9]
Hiromi S**ETA**,[25] Megumi S**HIDATSU**,[59] Aurora S**IMIONESCU**,[22]
Randall K. S**MITH**,[16] Yang S**OONG**,[9] Łukasz S**TAWARZ**,[74] Yasuharu S**UGAWARA**,[22]
Satoshi S**UGITA**,[50] Andrew S**ZYMKOWIAK**,[20] Hiroyasu T**AJIMA**,[5]
Hiromitsu T**AKAHASHI**,[28] Tadayuki T**AKAHASHI**,[22] Shiníchiro T**AKEDA**,[63]
Yoh T**AKEI**,[22] Toru T**AMAGAWA**,[75] Takayuki T**AMURA**,[22] Takaaki T**ANAKA**,[52]
Yasuo T**ANAKA**,[76,22] Yasuyuki T. T**ANAKA**,[28] Makoto S. T**ASHIRO**,[77]
Yuzuru T**AWARA**,[41] Yukikatsu T**ERADA**,[77] Yuichi T**ERASHIMA**,[11]
Francesco T**OMBESI**,[9,39,78] Hiroshi T**OMIDA**,[22] Yohko T**SUBOI**,[49]
Masahiro T**SUJIMOTO**,[22] Hiroshi T**SUNEMI**,[42] Takeshi Go T**SURU**,[52]
Hiroyuki U**CHIDA**,[52] Hideki U**CHIYAMA**,[79] Yasunobu U**CHIYAMA**,[44]
Shutaro U**EDA**,[22] Yoshihiro U**EDA**,[23] Shiníchiro U**NO**,[80] C. Megan U**RRY**,[20]
Eugenio U**RSINO**,[31] Shin W**ATANABE**,[22] Norbert W**ERNER**,[81,82,28]
Dan R. W**ILKINS**,[6] Brian J. W**ILLIAMS**,[58] Shinya Y**AMADA**,[25]
Hiroya Y**AMAGUCHI**,[9,57] Kazutaka Y**AMAOKA**,[5,41] Noriko Y. Y**AMASAKI**,[22]
Makoto Y**AMAUCHI**,[40] Shigeo Y**AMAUCHI**,[67] Tahir Y**AQOOB**,[9,39]
Yoichi Y**ATSU**,[50] Daisuke Y**ONETOKU**,[27] Irina Z**HURAVLEVA**,[6,7] and
Abderahmen Z**OGHBI**[62]

[1]Dublin Institute for Advanced Studies, 31 Fitzwilliam Place, Dublin 2, Ireland
[2]Max-Planck-Institut für Kernphysik, P.O. Box 103980, 69029 Heidelberg, Germany
[3]Gran Sasso Science Institute, viale Francesco Crispi, 7 67100 L'Aquila (AQ), Italy
[4]SRON Netherlands Institute for Space Research, Sorbonnelaan 2, 3584 CA Utrecht, The Netherlands
[5]Institute for Space-Earth Environmental Research, Nagoya University, Furo-cho, Chikusa-ku, Nagoya,
 Aichi 464-8601, Japan
[6]Kavli Institute for Particle Astrophysics and Cosmology, Stanford University, 452 Lomita Mall, Stanford,
 CA 94305, USA
[7]Department of Physics, Stanford University, 382 Via Pueblo Mall, Stanford, CA 94305, USA
[8]SLAC National Accelerator Laboratory, 2575 Sand Hill Road, Menlo Park, CA 94025, USA
[9]NASA, Goddard Space Flight Center, 8800 Greenbelt Road, Greenbelt, MD 20771, USA
[10]Department of Astronomy, University of Geneva, ch. d'Écogia 16, CH-1290 Versoix, Switzerland
[11]Department of Physics, Ehime University, 2-5 Bunkyo-cho, Matsuyama, Ehime 790-8577, Japan
[12]Department of Physics and Oskar Klein Center, Stockholm University, 106 91 Stockholm, Sweden
[13]Department of Physics, The University of Tokyo, 7-3-1 Hongo, Bunkyo-ku, Tokyo 113-0033, Japan
[14]Research Center for the Early Universe, School of Science, The University of Tokyo, 7-3-1 Hongo,
 Bunkyo-ku, Tokyo 113-0033, Japan
[15]Kavli Institute for Astrophysics and Space Research, Massachusetts Institute of Technology,
 77 Massachusetts Avenue, Cambridge, MA 02139, USA
[16]Smithsonian Astrophysical Observatory, 60 Garden St., MS-4. Cambridge, MA 02138, USA
[17]Lawrence Livermore National Laboratory, 7000 East Avenue, Livermore, CA 94550, USA
[18]Department of Physics and Astronomy, Wayne State University, 666 W. Hancock St, Detroit, MI 48201,
 USA
[19]Department of Astronomy, Yale University, New Haven, CT 06520-8101, USA

[20] Department of Physics, Yale University, New Haven, CT 06520-8120, USA

[21] Centre for Extragalactic Astronomy, Department of Physics, University of Durham, South Road, Durham, DH1 3LE, UK

[22] Japan Aerospace Exploration Agency, Institute of Space and Astronautical Science, 3-1-1 Yoshino-dai, Chuo-ku, Sagamihara, Kanagawa 252-5210, Japan

[23] Department of Astronomy, Kyoto University, Kitashirakawa-Oiwake-cho, Sakyo-ku, Kyoto, Kyoto 606-8502, Japan

[24] The Hakubi Center for Advanced Research, Kyoto University, Yoshida-honmachi, Sakyo-ku, Kyoto, Kyoto 606-8501, Japan

[25] Department of Physics, Tokyo Metropolitan University, 1-1 Minami-Osawa, Hachioji, Tokyo 192-0397, Japan

[26] Institute of Astronomy, University of Cambridge, Madingley Road, Cambridge, CB3 0HA, UK

[27] Faculty of Mathematics and Physics, Kanazawa University, Kakuma-machi, Kanazawa, Ishikawa 920-1192, Japan

[28] School of Science, Hiroshima University, 1-3-1 Kagamiyama, Higashi-Hiroshima, Hiroshima 739-8526, Japan

[29] Department of Physics, Tokyo University of Science, 1-3 Kagurazaka, Shinjuku-ku, Tokyo 162-8601, Japan

[30] Fujita Health University, 1-98 Dengakugakubo, Kutsukake-cho, Toyoake, Aichi 470-1192, Japan

[31] Physics Department, University of Miami, 1320 Campo Sano Dr., Coral Gables, FL 33146, USA

[32] Department of Astronomy and Physics, Saint Mary's University, 923 Robie Street, Halifax, NS, B3H 3C3, Canada

[33] Department of Physics and Astronomy, University of Southampton, Highfield, Southampton, SO17 1BJ, UK

[34] Laboratoire APC, 10 rue Alice Domon et Léonie Duquet, 75013 Paris, France

[35] CEA Saclay, 91191 Gif sur Yvette, France

[36] European Space Research and Technology Center, Keplerlaan 1 2201 AZ Noordwijk, The Netherlands

[37] Department of Physics and Astronomy, Aichi University of Education, 1 Hirosawa, Igaya-cho, Kariya, Aichi 448-8543, Japan

[38] Department of Physics, Tokyo University of Science, 2641 Yamazaki, Noda, Chiba 278-8510, Japan

[39] Department of Physics, University of Maryland Baltimore County, 1000 Hilltop Circle, Baltimore, MD 21250, USA

[40] Department of Applied Physics and Electronic Engineering, University of Miyazaki, 1-1 Gakuen Kibanadai-Nishi, Miyazaki, Miyazaki 889-2192, Japan

[41] Department of Physics, Nagoya University, Furo-cho, Chikusa-ku, Nagoya, Aichi 464-8602, Japan

[42] Department of Earth and Space Science, Osaka University, 1-1 Machikaneyama-cho, Toyonaka, Osaka 560-0043, Japan

[43] Department of Physics, Kwansei Gakuin University, 2-1 Gakuen, Sanda, Hyogo 669-1337, Japan

[44] Department of Physics, Rikkyo University, 3-34-1 Nishi-Ikebukuro, Toshima-ku, Tokyo 171-8501, Japan

[45] Department of Physics and Astronomy, Rutgers University, 136 Frelinghuysen Road, Piscataway, NJ 08854, USA

[46] Meisei University, 2-1-1 Hodokubo, Hino, Tokyo 191-8506, Japan

[47] Leiden Observatory, Leiden University, PO Box 9513, 2300 RA Leiden, The Netherlands

[48] Research Institute for Science and Engineering, Waseda University, 3-4-1 Ohkubo, Shinjuku-ku, Tokyo 169-8555, Japan

[49] Department of Physics, Chuo University, 1-13-27 Kasuga, Bunkyo-ku, Tokyo 112-8551, Japan

[50] Department of Physics, Tokyo Institute of Technology, 2-12-1 Ookayama, Meguro-ku, Tokyo 152-8550, Japan

[51] Department of Physics, Toho University, 2-2-1 Miyama, Funabashi, Chiba 274-8510, Japan

[52] Department of Physics, Kyoto University, Kitashirakawa-Oiwake-Cho, Sakyo-ku, Kyoto, Kyoto 606-8502, Japan

[53] European Space Astronomy Center, Camino Bajo del Castillo, s/n., 28692 Villanueva de la Cañada, Madrid, Spain

[54] Universities Space Research Association, 7178 Columbia Gateway Drive, Columbia, MD 21046, USA

[55] National Science Foundation, 4201 Wilson Blvd, Arlington, VA 22230, USA

[56] Department of Electronic Information Systems, Shibaura Institute of Technology, 307 Fukasaku, Minuma-ku, Saitama, Saitama 337-8570, Japan

[57] Department of Astronomy, University of Maryland, College Park, MD 20742, USA

[58] Space Telescope Science Institute, 3700 San Martin Drive, Baltimore, MD 21218, USA

[59] Institute of Physical and Chemical Research, 2-1 Hirosawa, Wako, Saitama 351-0198, Japan

[60] Department of Physics, University of Wisconsin, Madison, WI 53706, USA

[61] Department of Physics and Astronomy, University of Waterloo, 200 University Avenue West, Waterloo, Ontario, N2L 3G1, Canada

[62] Department of Astronomy, University of Michigan, 1085 South University Avenue, Ann Arbor, MI 48109, USA

[63] Okinawa Institute of Science and Technology Graduate University, 1919-1 Tancha, Onna-son, Kunigami-gun, Okinawa 904-0495, Japan

[64] Hiroshima Astrophysical Science Center, Hiroshima University, 1-3-1 Kagamiyama, Higashi-Hiroshima, Hiroshima 739-8526, Japan

[65] Faculty of Liberal Arts, Tohoku Gakuin University, 2-1-1 Tenjinzawa, Izumi-ku, Sendai, Miyagi 981-3193, Japan

[66] Faculty of Science, Yamagata University, 1-4-12 Kojirakawa-machi, Yamagata, Yamagata 990-8560, Japan

[67] Department of Physics, Nara Women's University, Kitauoyanishi-machi, Nara, Nara 630-8506, Japan

[68] Department of Teacher Training and School Education, Nara University of Education, Takabatake-cho, Nara, Nara 630-8528, Japan

[69] Frontier Research Institute for Interdisciplinary Sciences, Tohoku University, 6-3 Aramaki-aza-aoba, Aoba-ku, Sendai, Miyagi 980-8578, Japan

[70] Astronomical Institute, Tohoku University, 6-3 Aramaki-aza-aoba, Aoba-ku, Sendai, Miyagi 980-8578, Japan

[71] Astrophysics Laboratory, Columbia University, 550 West 120th Street, New York, NY 10027, USA

[72] Department of Physics and Astronomy, University of Manitoba, Winnipeg, MB R3T 2N2, Canada

[73] Department of Physics and Mathematics, Aoyama Gakuin University, 5-10-1 Fuchinobe, Chuo-ku, Sagamihara, Kanagawa 252-5258, Japan

[74] Astronomical Observatory of Jagiellonian University, ul. Orla 171, 30-244 Kraków, Poland

[75] RIKEN Nishina Center, 2-1 Hirosawa, Wako, Saitama 351-0198, Japan

[76] Max-Planck-Institut für extraterrestrische Physik, Giessenbachstrasse 1, 85748 Garching, Germany

[77] Department of Physics, Saitama University, 255 Shimo-Okubo, Sakura-ku, Saitama, Saitama 338-8570, Japan

[78] Department of Physics, University of Rome "Tor Vergata", Via della Ricerca Scientifica 1, I-00133 Rome, Italy

[79] Faculty of Education, Shizuoka University, 836 Ohya, Suruga-ku, Shizuoka, Shizuoka 422-8529, Japan

[80] Faculty of Health Sciences, Nihon Fukushi University , 26-2 Higashi Haemi-cho, Handa, Aichi 475-0012, Japan

[81] MTA-Eötvös University Lendület Hot Universe Research Group, Pázmány Péter sétány 1/A, Budapest, 1117, Hungary

[82] Department of Theoretical Physics and Astrophysics, Faculty of Science, Masaryk University, Kotlářská 2, Brno, 611 37, Czech Republic

*Corresponding authors: Shinya Nakashima, Kyoko Matsushita, Aurora Simionescu, Mark Bautz, Kazuhiro Nakazawa, Takashi Okajima, and Noriko Yamasaki.

†E-mail: shinya.nakashima@riken.jp

Abstract

The present paper explains the temperature structure of X-ray emitting plasma in the core of the Perseus cluster based on 1.8–20.0 keV data obtained with the Soft X-ray Spectrometer (SXS) on board the Hitomi Observatory. A series of four observations was carried out, with a total effective exposure time of 338 ks that covered a central region of $\sim$7′ in diameter. SXS was operated with an energy resolution of $\sim$5 eV (full width at half maximum) at 5.9 keV. Not only fine structures of K-shell lines in He-like ions, but also transitions from higher principal quantum numbers were clearly resolved from Si through Fe. That enabled us to perform temperature diagnostics using the line ratios of Si, S, Ar, Ca, and Fe, and to provide the first direct measurement of the excitation temperature and ionization temperature in the Perseus cluster. The observed spectrum is roughly reproduced by a single-temperature thermal plasma model in collisional ionization equilibrium, but detailed line-ratio diagnostics reveal slight deviations from this approximation. In particular, the data exhibit an apparent trend of increasing ionization temperature with the atomic mass, as well as small differences between the ionization and excitation temperatures for Fe, the only element for which both temperatures could be measured. The best-fit two-temperature models suggest a combination of 3 and 5 keV gas, which is consistent with the idea that the observed small deviations from a single-temperature approximation are due to the effects of projecting the known radial temperature gradient in the cluster core along the line of sight. A comparison with the Chandra/ACIS and the XMM-Newton/RGS results, on the other hand, suggests that additional lower-temperature components are present in the intracluster medium (ICM), but not detectable with Hitomi/SXS giving its 1.8–20 keV energy band.

Key words: galaxies: clusters: individual (Perseus) — methods: observational — X-rays: galaxies: clusters

1 Introduction

The X-ray emitting hot intracluster medium (ICM) dominates the baryonic mass in galaxy clusters, and its thermodynamical properties are crucial for studying the evolution of large-scale structure in the Universe. Discontinuities in the ICM temperature and density profiles reveal ongoing cluster mergers (Markevitch et al. 2000; Vikhlinin et al. 2001; Markevitch & Vikhlinin 2007; Akamatsu & Kawahara 2013), while pressure profiles in the cluster outskirts are also the key to an understanding of their growth (Arnaud et al. 2010; Simionescu et al. 2011; Planck Collaboration 2013; Simionescu et al. 2017). The thermodynamical properties of the dense ICM at the centers of "cool-core" clusters are even more complex: despite the fact that radiative cooling in these regions should be very efficient, stars are being formed at a rate smaller than that expected from the amount of hot ICM (e.g., Peterson et al. 2003). The heating mechanism responsible for compensating the radiative cooling is under debate, and various ideas have been proposed, such as feedback from the active galactic nuclei (AGN) in the brightest cluster

galaxies (e.g., McNamara & Nulsen 2007), energy transfer from moving member galaxies (e.g, Makishima et al. 2001; Gu et al. 2013), and cosmic-ray streaming with Alfvén waves (e.g., Fujita et al. 2013). While being less effective than expected, some radiative cooling likely does occur, and the presence of multiphase ICM in cool-core clusters is also reported (Fukazawa et al. 1994; Sanders & Fabian 2007; Takahashi et al. 2009; Gu et al. 2012; Sanders et al. 2016; Pinto et al. 2016).

To date, temperature measurements of the ICM have been mainly performed by fitting broad-band spectra (typically 0.5–10.0 keV band) obtained from X-ray CCDs. Because of the moderate energy resolution of this type of spectrometer, temperatures are mainly determined based on the shapes of the continuum and the Fe L-shell lines complex. However, the continuum shape is subject to uncertainties due to background modeling and/or effective area calibration (e.g., de Plaa et al. 2007; Leccardi & Molendi 2008; Nevalainen et al. 2010; Schellenberger et al. 2015).

An independent estimate of the gas temperature can be obtained from the flux ratios of various emission lines, the

"line ratio diagnostics"; the ratio between different transitions in the same ion, such as Lyα-to-Lyβ, indicates the excitation temperature, and the ratio of lines from different ionization stages, such as Heα-to-Lyα, represents the ion fraction (also referred to as the ionization temperature). These temperatures should match the temperature from the continuum shape when the observed plasma is a truly single temperature in collisional ionization equilibrium (CIE). If there is some disagreement between those temperatures, a deviation from a single CIE plasma is suggested: multi-temperature and/or non-equilibrium ionization (NEI). For instance, Matsushita et al. (2002) utilized the Si and S K-shell lines to measure the temperature profile in M 87. The ratios of the K-shell lines from Fe were used for the Ophiuchus cluster (Fujita et al. 2008), the Coma cluster (Sato et al. 2011), and Abell 754 (Inoue et al. 2016). In practice, this method has been applied to a relatively small number of lines because of line blending, and also because only the fluxes of the strongest lines are free from uncertainties in the exact continuum calibration and background subtraction.

The XMM-Newton Reflection Grating Spectrometers (RGSs) offer higher spectral resolution, and enable us to perform diagnostics with O K-shell and Fe L-shell lines, which are sensitive to the temperature range $kT < 1$ keV (e.g., Pinto et al. 2016). However, the energy band of the RGS is limited to energies below 2 keV, and the energy resolution in diffuse sources is degraded due to the dispersive and slitless nature of these spectrometers. Therefore, observations with a non-dispersive high-resolution spectrometer covering a broad energy band are desired for a precise characterization of the multi-temperature structure in the ICM.

The Hitomi satellite launched in 2016 February performed the first cluster observations of this kind, using its Soft X-ray Spectrometer (SXS). This non-dispersive microcalorimeter achieved a spectral resolution of ∼5 eV in orbit (Porter et al. 2018), and observed the core of the Perseus cluster as its first-light target. In the observed region, fine ICM substructures, such as bubbles, ripples, and weak shock fronts, had previously been revealed by deep Chandra imaging (Fabian et al. 2011, and references therein). These features are thought to be due to the activity of the AGN in the cD galaxy NGC 1275, which is pumping out relativistic electrons that disturb and heat the surrounding X-ray gas. The presence of multiple-phase structure in the ICM spanning a temperature range of $kT = 0.5$–8 keV is also reported (Sanders & Fabian 2007; Pinto et al. 2016).

The first measurement of Doppler shift and Doppler broadening of the Fe-K emission lines from the Hitomi first-light data, reported in Hitomi Collaboration (2016) (hereafter First paper), revealed that the line-of-sight velocity dispersion of the ICM in the core regions is unexpectedly low and subsonic. Constraints on an unidentified feature at

3.5 keV, suggesting that it originates from dark matter (e.g., Bulbul et al. 2014), are described by Hitomi Collaboration (2017a). Using the full set of the Perseus data and the latest calibration, we performed X-ray spectroscopy over the full Hitomi SXS band, and report on a series of follow-up papers. In this paper, we concentrate on measurements of the temperature structure in the cluster core. The high spectral resolution of the SXS allowed us to estimate the gas temperature based on seventeen independent line ratios from various chemical elements (Si through Fe). Companion papers report results on the metal abundances (Hitomi Collaboration 2017b, henceforth Z paper), velocity fields (Hitomi Collaboration 2018a, V paper), properties of the AGN in NGC 1275 (Hitomi Collaboration 2018d, AGN paper), the atomic code comparison (Hitomi Collaboration 2018c, Atomic paper), and the detection of resonance scattering (Hitomi Collaboration 2018b, RS paper).

Throughout this paper, we assume a cluster redshift of 0.017284 (see appendix 1 of V paper) and a Hubble constant of 70 km s^{-1} Mpc^{-1}. Therefore, 1′ corresponds to a physical scale of 21 kpc. We use the 68% (1σ) confidence level for errors, but upper and lower limits are shown at the 99.7% (3σ) confidence level. The X-ray energies in spectra are denoted at the observed (hence, redshifted) frame rather than the object's rest-frame.

2 Observation and data reduction

2.1 Hitomi observation

We observed the Perseus cluster four times with Hitomi/SXS during the commissioning phase in 2016 February and March (table 1). The aim points of individual observations are shown in figure 1. The first-light observation of Hitomi (obs1) was offset by ∼3′ from the center of the Perseus cluster, because the attitude control system had not been commissioned at that time. In the next observation (obs2), the pointing direction was adjusted so that the Perseus core would be in the SXS field-of-view (FoV). The same region was observed again after an extension of the Hitomi Hard X-ray Detector's optical bench (obs3). The obs3 data were divided into the three sequential sets (100040030, 100040040, and 100040050) solely for convenience in pipeline processing. In the final observation (obs4), the aim point was fine tuned again to place the Perseus core in the center of the SXS FoV.

The SXS sensor is a (6 × 6)-pixel array (Kelley et al. 2018). Combined with the X-ray focusing mirror (Okajima et al. 2016), the SXS has a 3′ × 3′ FoV with an angular resolution of 1.′2 (half-power diameter). One corner pixel is always illuminated by a dedicated ^{55}Fe source to track the gain variation with the detector temperature, and is not used for astrophysical spectra. The SXS achieved

Table 1. List of observations.

| Name	Observation ID	$\alpha_{J2000.0}$ (°)	$\delta_{J2000.0}$ (°)	Observation date	Effective exposure (ks)
		Hitomi/SXS			
obs1	100040010	49.878	41.484	2016-02-24–2016-02-25	49
obs2	100040020	49.935	41.519	2016-02-25–2016-02-27	97
obs3	100040030, 100040040, 100040050	49.936	41.520	2016-03-04–2016-03-06	146
obs4	100040060	49.955	41.512	2016-03-06–2016-03-07	46
		Chandra/ACIS-I			
...	11714	49.928	41.569	2009-12-07–2009-12-08	92
		XMM-Newton/RGS			
...	0085110101, 0085110201	49.951	41.512	2001-01-30–2001-01-31	72
...	0305780101	49.950	41.513	2006-01-29–2006-01-31	125
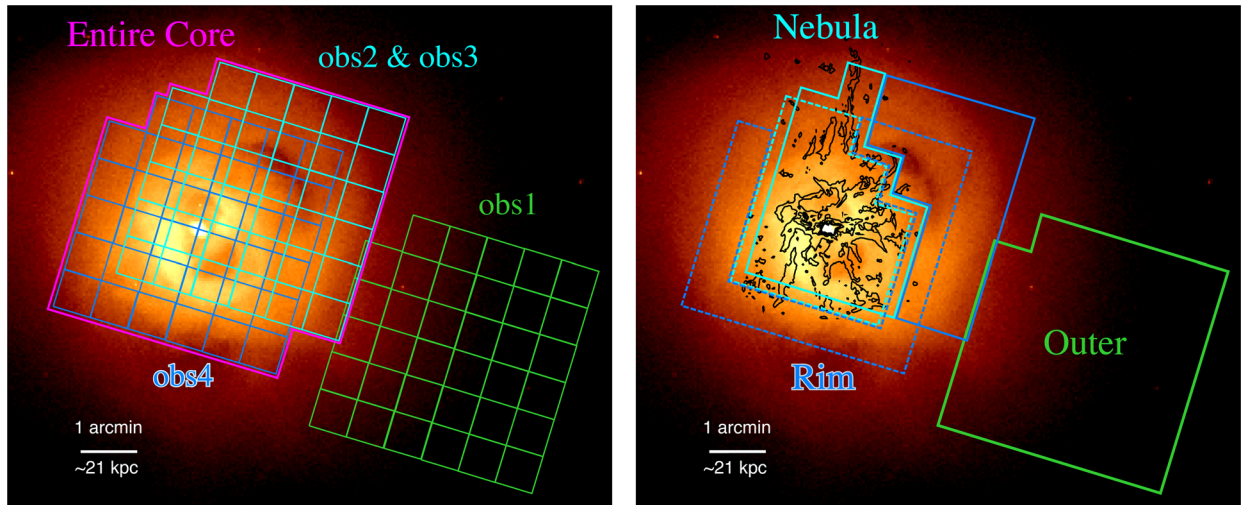
Fig. 1. (Left) SXS FoVs of the Hitomi observations overlaid on the Chandra X-ray color image in the 1.8–9.0 keV band. The green, cyan, and blue polygons indicate obs1, obs2 and obs3, and obs4, respectively. The 35 square boxes in each FoV correspond to the SXS pixels. The Entire Core region covering the whole obs2/obs3 and obs4 is also shown in magenta. (Right) Analysis regions used in subsection 3.3 overlaid on the same Chandra image. The Hα emission obtained with the WIYN 3.5 m telescope (Conselice et al. 2001) is also shown in the black contours. The cyan, blue, and green polygons correspond to the Nebula, Rim, and Outer regions, respectively. For the Nebula and Rim regions, we used slightly different sky regions between obs2/obs3 and obs4; the regions with solid lines are for obs2/obs3, and those with dashed lines are for obs4 (see text for details).

an unprecedented energy resolution of 5 eV (full width at half maximum) at 5.9 keV in orbit (Porter et al. 2018). The required energy bandpass of the SXS was 0.3–12 keV. During the early-mission observations discussed here, a gate valve remained closed to minimize the risk of contamination from outgassing in the spacecraft. The valve includes a Be window that absorbs most X-rays below 2 keV (Eckart et al. 2018).

The other instruments on Hitomi (Takahashi et al. 2018) still were not operational during most, or all, of the Perseus observations described here.

2.2 Hitomi data reduction

We used a cleaned event list provided by the pipeline processing version 03.01.006.007, and applied the additional screening described below using the HEAsoft version 6.21, Hitomi software version 6, and Hitomi calibration database version 7[1] (Angelini et al. 2017).

The SXS recorded signals up to 32 keV, but the standard pipeline processing reduced the energy coverage to the 0–16 keV band in order to achieve a sufficiently fine energy bin with a realistic number of channels in the nominal energy band (32768 bins with 0.5 eV bin^{-1}). However, the SXS was sensitive to bright sources above 16 keV because of its very low non-X-ray background (Kilbourne et al. 2017). We thus used a coarser bin size of 1.0 eV bin^{-1} to extend the energy coverage up to 32 keV instead. This was technically achieved by the sxsextend ftools task. We

---

[1] See ⟨https://heasarc.gsfc.nasa.gov/docs/hitomi/analysis⟩ for the Hitomi software and calibration database.

confirmed that our choice of the coarser bin size has no impact on our analysis due to intrinsic thermal and velocity broadening of lines.

We then applied event screening based on the pulse rise time versus the energy relationship tuned for a wider energy coverage.[2] We also selected only high primary grade events, for which the arrival time between the signal pulses was sufficiently large, and hence the best spectroscopic performance was achieved. The branching ratio to other grades was less than 2% for the Perseus observations, so this grade selection hardly reduced the effective exposure.

Since in-flight calibration of the SXS is limited, there is an uncertainty of the gain scale, especially at energies far from 5.9 keV. In addition, the SXS was not in thermal equilibrium during obs1 and obs2, and thus an ∼2 eV gain shift was seen even at 5.9 keV (Fujimoto et al. 2017). In order to correct for the gain scale, we applied a pixel-by-pixel redshift correction and a gain correction using a parabolic function, described in appendix 1.

We defined the four spectral analysis regions shown as the colour polygons in figure 1. The Entire Core region is the sum of the FoVs of obs2, obs3, and obs4 to maximize the photon statistics. In order to investigate the spatial variation of the temperature, we divided the Entire Core region into two sub-regions: the Nebula region associated with the Hα nebula (Conselice et al. 2001), and the Rim region located just outside the core, including the bubble seen to the northwest of the cluster center. The aim point of obs4 is different from that of obs2/3 by ∼60″; thus, for the Nebula and Rim regions, spectra of obs2/3 and obs4 were extracted using slightly different spatial regions, and later co-added. Lastly the fourth region, which we refer to as the Outer region, is the entire FoV of obs1.

Non-X-ray backgrounds (NXB) corresponding to each region were produced from the Earth-eclipsed durations by using `sxsnxbgen`. The redistribution matrix file (RMF) and the auxiliary response file (ARF) for spectral analysis were generated by `sxsmkrmf` and `aharfgen`, respectively. As an input to the ARF generator, we used the 1.8–9.0 keV Chandra image in which the AGN region ($r = 10″$) is replaced with average adjacent brightness. The spectrum of the Entire Core region with the corresponding non-X-ray background is shown in figure 2. The cluster is clearly detected above the NXB up to 20 keV. The attenuation below ∼2 keV due to the closed gate valve can also be seen. For our analysis, we thus focus on the energy band spanning a range of 1.8–20.0 keV.
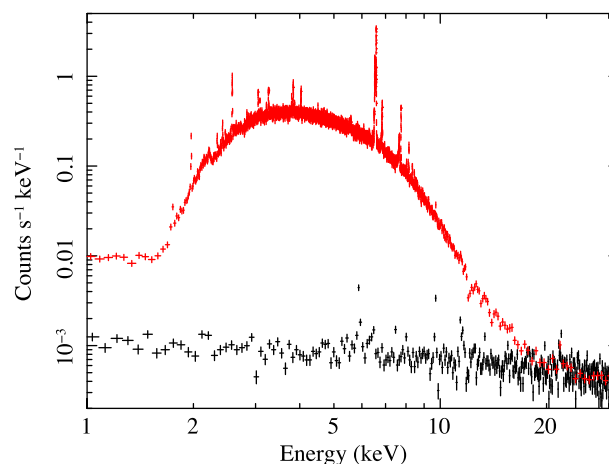

Fig. 2. SXS 1–32 keV spectrum in the Entire Core region (red). The corresponding non-X-ray background estimated by `sxsnxbgen` is also plotted in black. (Color online)

2.3 Chandra and XMM-Newton archive data

For comparison with the Hitomi results, we also analyzed archival data from Chandra and XMM-Newton. Details of the observations are summarized in table 1.

We reprocessed the Chandra data with the CIAO version 4.9 software package and calibration database version 4.7.4. Spectra were extracted from the Nebula and Rim regions, shown in figure 1. A 9″-radius circle around the central AGN region was excluded from the analysis, taking advantage of Chandra's spatial resolution. The spectra were binned so that each bin would include at least 100 counts. Background spectra were generated from the blank-sky observations provided in the calibration database, and were scaled so that their count rates in the 10–12 keV band would match the source spectra.

We followed the data analysis method of the CHEERS collaboration (de Plaa et al. 2017) for reduction of the XMM-Newton/RGS data with the SAS version 14.0.0 software package. We extracted RGS source spectra in a region centered on the peak of the source emission, with a width of 0.′8 in the cross-dispersion direction. While this is much smaller than the region probed by the SXS, a narrower extraction region in the cross-dispersion direction provides spectra that are least broadened by the spatial extent of the source, and thus have the best resolution. To further correct for this broadening, we used the `lpro` model component in SPEX to convolve the spectral models with the surface brightness profile extracted from the XMM-Newton MOS1 detector. We used background spectra generated by the SAS `rgsbkgmodel` task. The template background files were scaled using the count rates measured in the off-axis region of CCD9, in which the soft protons dominate the light curve.

---

[2] See the Hitomi data reduction guide for details ⟨https://heasarc.gsfc.nasa.gov/docs/hitomi/analysis⟩.

Fig. 3. SXS spectra extracted from the Entire Core region in the 1.8–3.0 keV (top), 3.0–4.8 keV (middle), and 6.4–8.5 keV (bottom) bands. The fitting phenomenological models are shown by the red solid curves. The Gaussians included in the model are also plotted by the black-dotted lines. (Color online)

3 Analysis and results

The procedures described below were used for the spectral analysis presented in this section, unless stated otherwise. Spectral fits were performed using the Xspec 12.9.1h

package (Arnaud 1996) employing the modified C-statistic (Cash 1979) in which a Poisson background spectrum is taken into account (also referred to as the W-statistic). We used the atomic databases of the AtomDB version 3.0.9 (Foster et al. 2012) and SPEXACT version 3.03.00 (Kaastra et al. 1996) for calculations of plasma models. We took differences between the model predictions as an estimate of model uncertainties. A python program was used to generate APEC format table models from SPEX,[3] allowing us to make a direct comparison of the results using a consistent treatment of all other assumptions and fit procedures.

Photoelectric absorption by cold matter in our Galaxy was modeled using the TBabs code version 2.3 (Wilms et al. 2000), in which fine-structures of absorption edges and cross-sections of dust grains and molecules were included. Its hydrogen column density was fixed at 1.38×10^{21} cm^{-2} in accordance with the all-sky H I survey (Kalberla et al. 2005). We also considered the contaminating emission from the AGN in NGC 1275. Its spectrum was modeled using a power-law continuum and a neutral Fe Kα line with parameters fixed at the values described in AGN paper. Its flux was estimated by ray-tracing simulations (aharfgen).

3.1 Line ratio diagnostics

Figure 3 shows the spectra extracted from the Entire Core region, focusing on the 1.8–3.0 keV, 3.0–4.8 keV, and 6.4–8.5 keV bands. Both the Heα and Lyα emission lines of Si, S, Ar, Ca, and Fe were detected and resolved. Furthermore, some transitions from higher principal quantum numbers were also resolved: up to ϵ ($n = 6$) from Fe in particular.

In order to derive the observed fluxes of these lines, we fitted the spectra in the three energy bands listed above with a phenomenological model consisting of continuum emission and Gaussian lines. We used a CIE plasma model based on AtomDB (the apec model) in which the strong lines listed in table 2 were replaced with Gaussians. In accordance with the First paper, the metal abundance of the plasma model was fixed at 0.62 solar and the line-of-sight velocity dispersion was fixed at 146 km s^{-1} to represent weaker emission lines not listed in table 2. Even when these parameters were varied by $\pm20\%$ (much higher than statistical errors shown in the Z paper and V paper), there was no significant impact on our line flux measurements. Doublets of the Lyman series were not resolved, except for Fe XXVI Lyα, and hence their centroid energies, line widths, and flux ratios were tied as shown in table 2. The line centroids and widths for Fe XXV Heβ_1 and Fe XXV Heβ_2 were also tied, as described in table 2. Unresolved structures

---

[3] ⟨http://www.mpe.mpg.de/jsanders/code/⟩.

Table 2. List of lines considered for the Gaussian fit.*

Line name	E_0[†]	Constraints			
	(eV)	Tied to	Center	Width	Flux
Si XIII w	1865.0	—	—	—	—
Si XIV Lyα_1	2006.1	—	—	—	—
Si XIV Lyα_2	2004.3	Si XIV Lyα_1	-1.8 eV	$\times 1.0$	$\times 0.5$
Si XIV Lyβ_1	2376.6	—	—	—	—
Si XIV Lyβ_2	2376.1	Si XIV Lyβ_1	-0.5 eV	$\times 1.0$	$\times 0.5$
S XV w	2460.6	—	—	—	—
S XVI Lyα_1	2622.7	—	—	—	—
S XVI Lyα_2	2619.7	S XVI Lyα_1	-3.0 eV	$\times 1.0$	$\times 0.5$
S XVI Lyβ_1	3106.7	—	—	—	—
S XVI Lyβ_2	3105.8	S XVI Lyβ_1	-0.9 eV	$\times 1.0$	$\times 0.5$
S XVI Lyγ_1	3276.3	—	—	—	—
S XVI Lyγ_2	3275.9	S XVI Lyγ_1	-0.4 eV	$\times 1.0$	$\times 0.5$
Ar XVII w	3139.6	—	—	—	—
Ar XVIII Lyα_1	3323.0	—	—	—	—
Ar XVIII Lyα_2	3318.2	Ar XVIII Lyα_1	-4.8 eV	$\times 1.0$	$\times 0.5$
Ar XVIII Lyβ_1	3935.7	—	—	—	—
Ar XVIII Lyβ_2	3934.3	Ar XVIII Lyβ_1	-1.4 eV	$\times 1.0$	$\times 0.5$
Ca XIX w	3902.4	—	—	—	—
Ca XIX Heβ_1[‡]	4583.5	—	—	—	—
Ca XX Lyα_1	4107.5	—	—	—	—
Ca XX Lyα_2	4100.1	Ca XX Lyα_1	-7.4 eV	$\times 1.0$	$\times 0.5$
Fe XXV z	6636.6	—	—	—	—
Fe XXV w	6700.4	—	—	—	—
Fe XXV Heβ_1	7881.5	—	—	—	—
Fe XXV Heβ_2	7872.0	Fe XXV Heβ_1	-9.5 eV	$\times 1.0$	—
Fe XXV Heγ_1[‡]	8295.5	—	—	—	—
Fe XXV Heδ_1[‡]	8487.4	—	—	—	—
Fe XXV Heϵ_1[‡]	8588.5	—	—	—	—
Fe XXVI Lyα_1	6973.1	—	—	—	—
Fe XXVI Lyα_2	6951.9	Fe XXVI Lyα_1	—	$\times 1.0$	—
Fe XXVI Lyβ_1	8252.6	—	—	—	—
Fe XXVI Lyβ_2	8246.4	Fe XXVI Lyβ_1	-6.2 eV	$\times 1.0$	—
Ni XXVII w	7805.6	—	—	—	—
		Constraints only on the Rim region			
Si XIII w	1865.0	Si XIV Lyα_1	fixed at E_0	$\times 1.0$	—
Ca XIX Heβ_1	4583.5	Ca XX Lyα_1	fixed at E_0	$\times 1.0$	—
		Constraints only on the Outer region			
Si XIII w	1865.0	Si XIV Lyα_1	fixed at E_0	$\times 1.0$	—
S XV w	2460.6	S XVI Lyα_1	fixed at E_0	$\times 1.0$	—
Ca XIX Heβ_1	4583.5	Ca XX Lyα_1	fixed at E_0	$\times 1.0$	—
Fe XXV Heγ_1	8295.5	Fe XXV Heβ_1	fixed at E_0	$\times 1.0$	—
Fe XXV Heδ_1	8487.4	Fe XXV Heβ_1	fixed at E_0	$\times 1.0$	—
Fe XXV Heϵ_1	8588.5	Fe XXV Heβ_1	fixed at E_0	$\times 1.0$	—

*Free parameters are denoted by the hyphen (-).

[†]Fiducial energies of the emission lines at the rest frame in `AtomDB 3.0.9`.

[‡]Ca XIX Heβ_2, Fe XXV Heγ_2, Fe XXV Heδ_2, and Fe XXV Heϵ_2 were omitted because their fluxes are too small to be constrained by the SXS spetra.

in Ca XIX Heβ, Fe XXV Heγ, Fe XXV Heδ, and Fe XXV Heϵ were represented by a single Gaussian. The Gaussian fluxes that we obtained are shown in table 3. The results of the line centroid and line width, though not relevant to our analysis, are summarized in appendix 2. Readers are referred to the V paper for a detailed discussion of the velocity dispersions and line-of-sight velocity shifts.

Assuming a single-temperature CIE plasma, and employing the `AtomDB` and `SPEXACT` databases, we calculated how the line ratios considered here depend on

Table 3. Observed line fluxes derived from Gaussian fits.*

Line name	Flux (10^{-5} ph cm^{-2} s^{-1})			
	Entire Core	Nebula	Rim	Outer
Si XIII w	$6.40^{+4.71}_{-2.67}$	$5.87^{+3.60}_{-2.54}$	<5.45	<4.54
Si XIV Lyα_1	$32.43^{+2.29}_{-2.23}$	$20.11^{+1.92}_{-1.83}$	$21.83^{+2.64}_{-2.52}$	$4.09^{+2.27}_{-1.72}$
Si XIV Lyβ_1	$6.96^{+0.91}_{-0.87}$	$5.03^{+0.74}_{-0.70}$	$3.93^{+1.04}_{-0.98}$	$1.21^{+0.82}_{-0.58}$
S XV w	$9.38^{+1.13}_{-1.11}$	$7.26^{+0.98}_{-0.99}$	$3.91^{+1.03}_{-0.94}$	<1.08
S XVI Lyα_1	$22.71^{+0.73}_{-0.72}$	$15.81^{+0.64}_{-0.63}$	$12.46^{+0.77}_{-0.76}$	$2.70^{+0.67}_{-0.64}$
S XVI Lyβ_1	$3.83^{+0.29}_{-0.29}$	$2.55^{+0.25}_{-0.24}$	$2.49^{+0.35}_{-0.33}$	$0.62^{+0.27}_{-0.22}$
S XVI Lyγ_1	$1.20^{+0.20}_{-0.19}$	$0.74^{+0.15}_{-0.17}$	$0.92^{+0.25}_{-0.24}$	$0.32^{+0.22}_{-0.17}$
Ar XVII w	$3.72^{+0.37}_{-0.36}$	$2.82^{+0.31}_{-0.30}$	$1.87^{+0.51}_{-0.47}$	$1.20^{+0.41}_{-0.34}$
Ar XVIII Lyα_1	$5.47^{+0.29}_{-0.29}$	$3.85^{+0.25}_{-0.25}$	$3.15^{+0.32}_{-0.30}$	$0.94^{+0.32}_{-0.30}$
Ar XVIII Lyβ_1	$0.77^{+0.15}_{-0.15}$	$0.51^{+0.12}_{-0.12}$	$0.63^{+0.20}_{-0.18}$	$0.26^{+0.15}_{-0.11}$
Ca XIX w	$5.20^{+0.27}_{-0.27}$	$3.66^{+0.23}_{-0.23}$	$2.94^{+0.30}_{-0.28}$	$0.93^{+0.29}_{-0.26}$
Ca XIX Heβ_1	$0.66^{+0.16}_{-0.10}$	$0.46^{+0.13}_{-0.10}$	$0.67^{+0.29}_{-0.35}$	$0.21^{+0.16}_{-0.12}$
Ca XX Lyα_1	$2.80^{+0.18}_{-0.15}$	$1.85^{+0.16}_{-0.15}$	$1.81^{+0.20}_{-0.19}$	$0.77^{+0.20}_{-0.19}$
Fe XXV w	$33.14^{+0.43}_{-0.34}$	$21.09^{+0.32}_{-0.31}$	$22.13^{+0.49}_{-0.35}$	$9.49^{+0.45}_{-0.44}$
Fe XXV z	$13.26^{+0.27}_{-0.25}$	$8.72^{+0.21}_{-0.22}$	$8.41^{+0.28}_{-0.27}$	$3.03^{+0.28}_{-0.27}$
Fe XXV Heβ_1	$4.73^{+0.12}_{-0.24}$	$2.80^{+0.12}_{-0.15}$	$3.35^{+0.19}_{-0.18}$	$1.49^{+0.21}_{-0.20}$
Fe XXV Heβ_2	$1.04^{+0.10}_{-0.18}$	$0.73^{+0.14}_{-0.08}$	$0.55^{+0.13}_{-0.12}$	<0.17
Fe XXV Heγ_1	$1.75^{+0.13}_{-0.13}$	$1.04^{+0.10}_{-0.10}$	$1.32^{+0.14}_{-0.13}$	$0.25^{+0.13}_{-0.12}$
Fe XXV Heδ_1	$0.88^{+0.12}_{-0.12}$	$0.55^{+0.10}_{-0.10}$	$0.63^{+0.13}_{-0.12}$	$0.27^{+0.13}_{-0.11}$
Fe XXV Heϵ_1	$0.54^{+0.10}_{-0.10}$	$0.34^{+0.08}_{-0.08}$	$0.43^{+0.12}_{-0.12}$	$0.15^{+0.12}_{-0.10}$
Fe XXVI Lyα_1	$3.68^{+0.16}_{-0.16}$	$2.24^{+0.13}_{-0.13}$	$2.68^{+0.17}_{-0.17}$	$1.35^{+0.22}_{-0.21}$
Fe XXVI Lyα_2	$2.17^{+0.14}_{-0.13}$	$1.31^{+0.12}_{-0.11}$	$1.59^{+0.14}_{-0.14}$	$0.99^{+0.20}_{-0.18}$
Fe XXVI Lyβ_1	$0.30^{+0.06}_{-0.06}$	$0.21^{+0.06}_{-0.05}$	$0.18^{+0.07}_{-0.04}$	$0.16^{+0.08}_{-0.06}$
Ni XXVII w	$1.43^{+0.13}_{-0.13}$	$1.01^{+0.11}_{-0.11}$	$0.79^{+0.13}_{-0.13}$	$0.43^{+0.16}_{-0.15}$

*The Lyα_2 lines of Si, S, Ar, and Ca are not shown because their parameter values are tied to Lyα_1 (see table 2 for details).

the temperature. The calculated temperature dependencies are shown in figure 4. The line emissivities used in these calculations are given in appendix 3 along with measurements of the emission measure, based on single line fluxes. Except for Fe Heϵ/z and Fe Lyα/Heϵ ratios, the two codes gave consistent values with each other within 5%–10% for the interesting temperature range, 1–7 keV. Detailed comparisons of line emissivities between the two codes are discussed in the Atomic paper.

A line ratio of different transitions in the same ion reflects the kinetic temperature of free electrons in the plasma, and is referred to as "excitation temperature," or T_e. Referring to figure 4, we calculated T_e from the observed line ratios of Lyβ/Lyα of Si and Ar, Lyγ/Lyα of S, Heβ/w of Ca, and Heβ/z, Heγ/z, Heδ/z, and Heϵ/z of Fe (top three rows of figure 4). S Lyβ was not used because it is not separated from Ar z, whose energy is 3102 eV (see figure 3). Fe Lyβ was not used because of the low observed flux.

Fluxes of Lyα_1 and Lyα_2 were co-added in this calculation. In the same manner, the fine structures of Lyβ, Lyγ, Heβ, Heγ, Heδ, and Heϵ were also summed. The interval of the observed line ratios and the corresponding temperature ranges are overlaid on figure 4 as color boxes.

Separately from the T_e diagnostics, we used line ratios of different ionization species to measure the ion fraction for each element. We parametrized these ratios by "ionization temperatures" or T_Z. When the emission comes from a single-component and optically thin plasma under the CIE, T_Z from every element should be the same as T_e. T_Z values were calculated using the line ratios of Lyα/w of Si, S, Ar, and Ca and Lyα/z, Lyα/Heβ, Lyα/Heγ, Lyα/Heδ, and Lyα/Heϵ of Fe (bottom three rows of figure 4). The temperature ranges derived from the observed line ratios are shown in figure 4.

We summarize the derived T_e and T_Z in figure 5. T_Z from Fe, which is determined with the smallest statistical uncertainties, has typical values of 4–5 keV. T_Z values from the Entire Core and Nebula regions are clearly different among elements; namely, there is a tendency of increasing T_Z with atomic number. These results indicate a deviation from a single-temperature CIE model. The T_Z value from the Rim region also suggests a slight deviation from a single-temperature model. The results of the Outer region are consistent with a single-temperature approximation.

The T_e values from Fe for the Nebula and Rim regions are ∼3 and 4 keV, respectively. In the Nebula and Entire Core regions, the T_e values from Fe are lower than T_Z at the 2σ–3σ level, providing further evidence for a deviation from the single-temperature approximation. For Si, S, Ar, and Ca, the line ratios that are sensitive to T_e are all consistent with the CIE prediction with a temperature of 2–4 keV within the statistical 1σ–2σ errors; however, the corresponding T_e is not constrained.

3.2 Modeling of the broad-band spectrum in the Entire Core region

We then tried to reproduce the broad-band (1.8–20.0 keV) spectrum with optically thin thermal plasma models based on AtomDB and SPEXACT. In the analysis of this section, we focus on the spectrum of the Entire Core region in order to ignore any contamination of photons scattered due to the point spread function (PSF) of the telescope, and to investigate any uncertainties due to the atomic codes and the effective area calibration.

3.2.1 Single-temperature plasma models
Although the SXS spectra indicate multi-temperature conditions, we began by fitting the data with the simplest model; that is, a single-temperature CIE plasma model
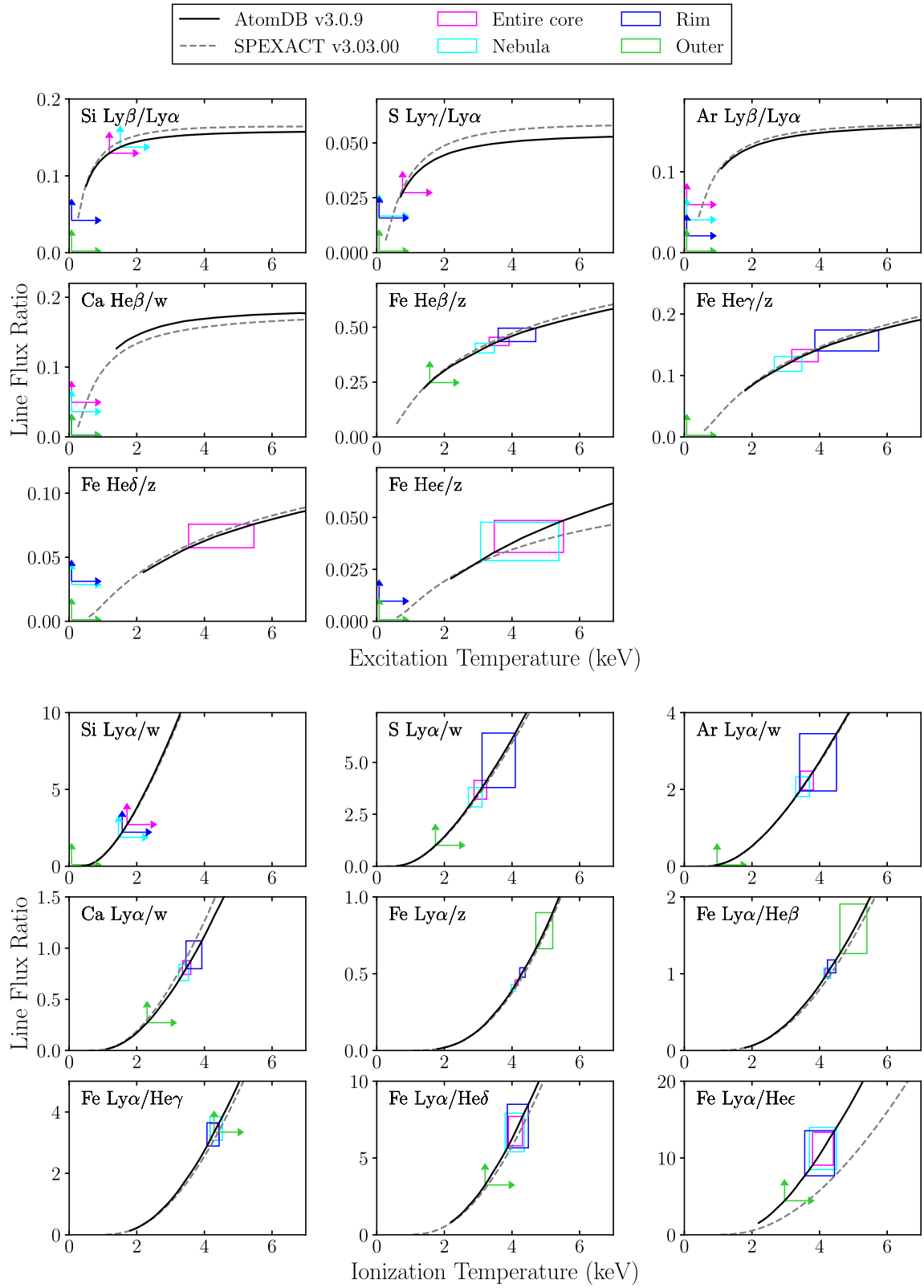
Fig. 4. Upper eight panels show the flux ratios of the emission lines as a function of the excitation temperature, calculated from `AtomDB` (black solid curve) and `SPEXACT` (gray-dashed curve) assuming a single-temperature CIE plasma. The lines used in the calculations are denoted in each panel. The color boxes show the ranges of the observed line ratios and the corresponding `AtomDB` temperatures at the 1σ confidence level. Magenta, blue, cyan, and green correspond to the Entire Core, Rim, Nebula, and Outer regions, respectively. When the ranges of the statistical errors of the observed line ratios are outside the models, 3σ lower limits are shown instead by the color arrows. The lower nine panels are the same as the upper panels, but for the ionization temperature.
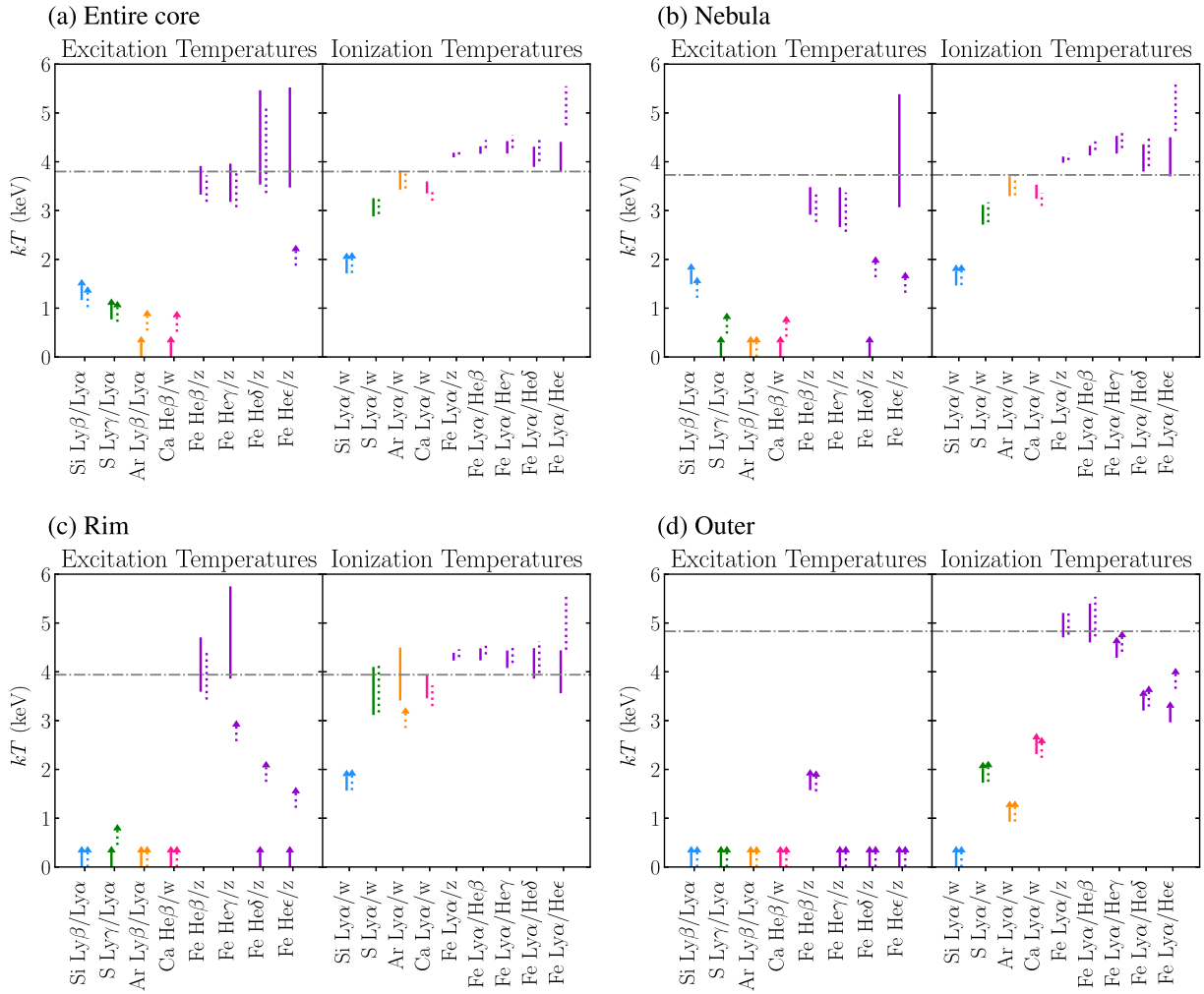
Fig. 5. Excitation temperatures and ionization temperatures derived from individual line ratios in (a) the Entire Core, (b) Nebula, (c) Rim, and (d) Outer regions. Cyan, green, orange, pink, and purple indicate Si, S, Ar, Ca, and Fe, respectively. The results based on AtomDB and SPEXACT are shown by the solid and dotted lines, respectively. The horizontal dot-dashed lines show the best-fit $kT_{\rm line}$ of the modified-1T model described in sub-subsection 3.2.1 and subsection 3.3. (Color online)

(hereafter, 1CIE model), with the temperature ($kT_{\rm 1CIE}$), the abundances of Si, S, Ar, Ca, Cr, Mn, Fe, and Ni, the line-of-sight velocity dispersion, and the normalization (N) as free parameters. The abundances of other elements from Li through Zn were tied to that of Fe. Since the resonance line of He-like Fe (Fe XXV w) is subject to the resonance scattering effect (see RS paper), we replaced it by a single Gaussian, so that it would not affect the parameters we obtained. The best-fit parameters are given in table 4; AtomDB and SPEXACT give consistent temperatures of 3.95 ± 0.01 keV and 3.94 ± 0.01 keV, respectively. The C-statistics are within the expected range that is calculated according to Kaastra (2017), and hence the fits are acceptable even in these simple models.

In the 1CIE fit, both the continuum shape and the emission-line flux are requisite to in the temperature determination. In order to fully utilize the line resolving power

of the SXS, we then modeled the continuum and lines separately, and determined the continuum temperatures ($kT_{\rm cont}$) and the line temperatures ($kT_{\rm line}$) (hereafter, the modified-1CIE model). In this model, $kT_{\rm cont}$ and $kT_{\rm line}$ were independently allowed to vary, whereas the other parameters were common (implemented as the bvvtapec model in Xspec). The best-fit parameters we obtained are shown in table 4. Both AtomDB and SPEXACT provide a reasonably good fit to the observed spectrum, as shown in figure 6. Compared to $kT_{\rm 1CIE}$, $kT_{\rm cont}$ and $kT_{\rm line}$ become slightly higher and lower, respectively, for both AtomDB and SPEXACT. Since $kT_{\rm cont}$ is closer to $kT_{\rm 1CIE}$ than $kT_{\rm line}$, the continuum shape most likely determines the temperature of the 1CIE model, rather than the line fluxes, even with high-resolution spectroscopy measurements. The temperature differences between AtomDB and SPEXACT are formally statistically significant, but are less than 0.1 keV.

Table 4. Best-fit parameters for the Entire Core region.

Model/parameter	AtomDB v3.0.9	SPEXACT v3.03.00
1CIE model		
kT_{1CIE} (keV)	$3.95^{+0.01}_{-0.01}$	$3.94^{+0.01}_{-0.01}$
N (10^{12} cm^{-5})	$23.20^{+0.05}_{-0.05}$	$22.78^{+0.04}_{-0.04}$
C-statistics/dof	13123.6/12979	13181.7/12979
Modified-1CIE model		
kT_{cont} (keV)	$4.01^{+0.01}_{-0.01}$	$3.95^{+0.01}_{-0.01}$
kT_{line} (keV)	$3.80^{+0.02}_{-0.02}$	$3.89^{+0.02}_{-0.02}$
N (10^{12} cm^{-5})	$22.77^{+0.04}_{-0.04}$	$22.67^{+0.05}_{-0.05}$
C-statistics/dof	13085.9/12978	13178.7/12978
2CIE model (modified CIE + CIE)		
kT_{cont1} (keV)	$3.66^{+0.01}_{-0.02}$	$3.40^{+0.02}_{-0.01}$
kT_{line1} (keV)	$3.06^{+0.04}_{-0.04}$	$2.92^{+0.03}_{-0.03}$
kT_2 (keV)	$4.51^{+0.02}_{-0.03}$	$4.73^{+0.02}_{-0.02}$
N_1 (10^{12} cm^{-5})	$12.98^{+0.05}_{-0.05}$	$13.27^{+0.13}_{-0.09}$
N_2 (10^{12} cm^{-5})	$9.71^{+0.06}_{-0.05}$	$9.45^{+0.07}_{-0.05}$
C-statistics/dof	13058.5/12976	13093.9/12976
Power-law DEM model		
α	$10.92^{+0.11}_{-0.11}$	$4.68^{+0.03}_{-0.03}$
kT_{max} (keV)	$4.01^{+0.06}_{-0.01}$	$4.29^{+0.01}_{-0.01}$
N (10^{12} cm^{-5})	$21.38^{+0.24}_{-0.24}$	$15.39^{+0.04}_{-0.04}$
C-statistics/dof	13123.4/12978	13147.6/12978
Gaussian DEM model		
kT_{mean} (keV)	$3.94^{+0.01}_{-0.01}$	$3.89^{+0.01}_{-0.01}$
σ (keV)	$0.60^{+0.08}_{-0.11}$	$1.01^{+0.05}_{-0.05}$
N (10^{12} cm^{-5})	$11.65^{+0.02}_{-0.02}$	$11.67^{+0.03}_{-0.03}$
C-statistics/dof	13121.1/12978	13138.7/12978

The difference between kT_{cont} and kT_{line} is at most 0.23 keV, but statistically significant. Since we found the multi-temperature structure based on the line ratio diagnostics (subsection 3.1), that difference is possible. However, an uncertainty in the effective area might also affect the results: the in-flight calibration of Hitomi was not completed because of its short lifetime. We therefore assessed this uncertainty using the modified ARF based on the ground telescope calibration (ARF$_{ground}$) and the actual Crab data (ARF$_{Crab}$). See appendix 4 for the detailed correction method. We fitted the modified-1CIE model using ARF$_{ground}$ and ARF$_{Crab}$. The correction of the ARF slightly affects the parameters of the AGN components as well (see table 4 of the AGN paper). Even though the differences are very small, we used the specific AGN parameter values corresponding to each assumed ARF in our fits. The temperatures and C-statistics we obtained are summarized in figure 7; kT_{cont} varies depending on ARF because the continuum shape is subject to the effective area shape. On the

other hand, the values of kT_{line} measured with different assumptions for the ARF remain consistent with each other. Therefore, kT_{line} provides the most robust estimate of the temperature from the SXS spectrum, assuming a single-phase model. In terms of the C-statistics, the ARF$_{Crab}$ gives the best fit, but this choice of ARF also results in the largest difference between kT_{cont} and kT_{line}. This illustrates the difficulty of an effective area calibration with the limited amount of available data.

Even though the AGN paper carefully modeled the AGN emission, the uncertainty of its model parameters and their impact on the best-fit temperature structure should also be considered. If the AGN model is slightly changed, kT_{cont} would again change, while kT_{line} would be less affected, as demonstrated with a comparison of different ARFs.

3.2.2 Two-temperature plasma models
The line-ratio diagnostics in subsection 3.1 actually indicate the presence of a multi-temperature structure in the Perseus cluster core. As a simple approximation of the deviations from a single thermal phase, we first used a two-temperature model, where another CIE model was added to the modified-1CIE model (hereafter, the 2CIE model). The free parameters of the additional CIE component were the temperature and the normalization, while the abundances and the line-of-sight velocity dispersion were tied to those of the primary component. The results are given in table 4. As expected, the C-statistics are significantly improved from those of the modified-1CIE model ($\Delta C = 30$–91). However, as shown in the bottom subpanels of figures 6b–6f, the continuum is almost the same and the differences of line emissivities are at most 10% compared to the 1CIE model. The temperatures and normalizations obtained with the two spectral codes are in reasonably good agreement, although some differences are statistically significant. The dominant component now has a temperature of $kT_{line} = 3.06 \pm 0.03$ keV from AtomDB, which is fully consistent with $kT_{line} = 3.06^{+0.03}_{-0.08}$ keV from SPEXACT. The second thermal component is from hotter gas with $kT_2 \sim 5$ keV: that is, for this component, SPEXACT gives a ~10% higher temperature than AtomDB, and a somewhat lower relative normalization [$N_2/(N_1 + N_2)$ of 31% with SPEXACT and 43% with AtomDB]. The temperatures derived from the 2CIE fit are consistent with the line-ratio diagnostics shown in figure 5: the ionization temperature of S is ~3 keV and that of Fe is ~4.5 keV. We also checked difference of the line-of-sight velocity dispersion between the lower and higher temperature components, but no significant difference was found (see appendix 5 for details).

In the same manner as in the modified-1CIE model (subsubsection 3.2.1), we examined the effect of different ARFs (ARF$_{ground}$ and ARF$_{Crab}$) for the 2CIE model. Figure 8 shows
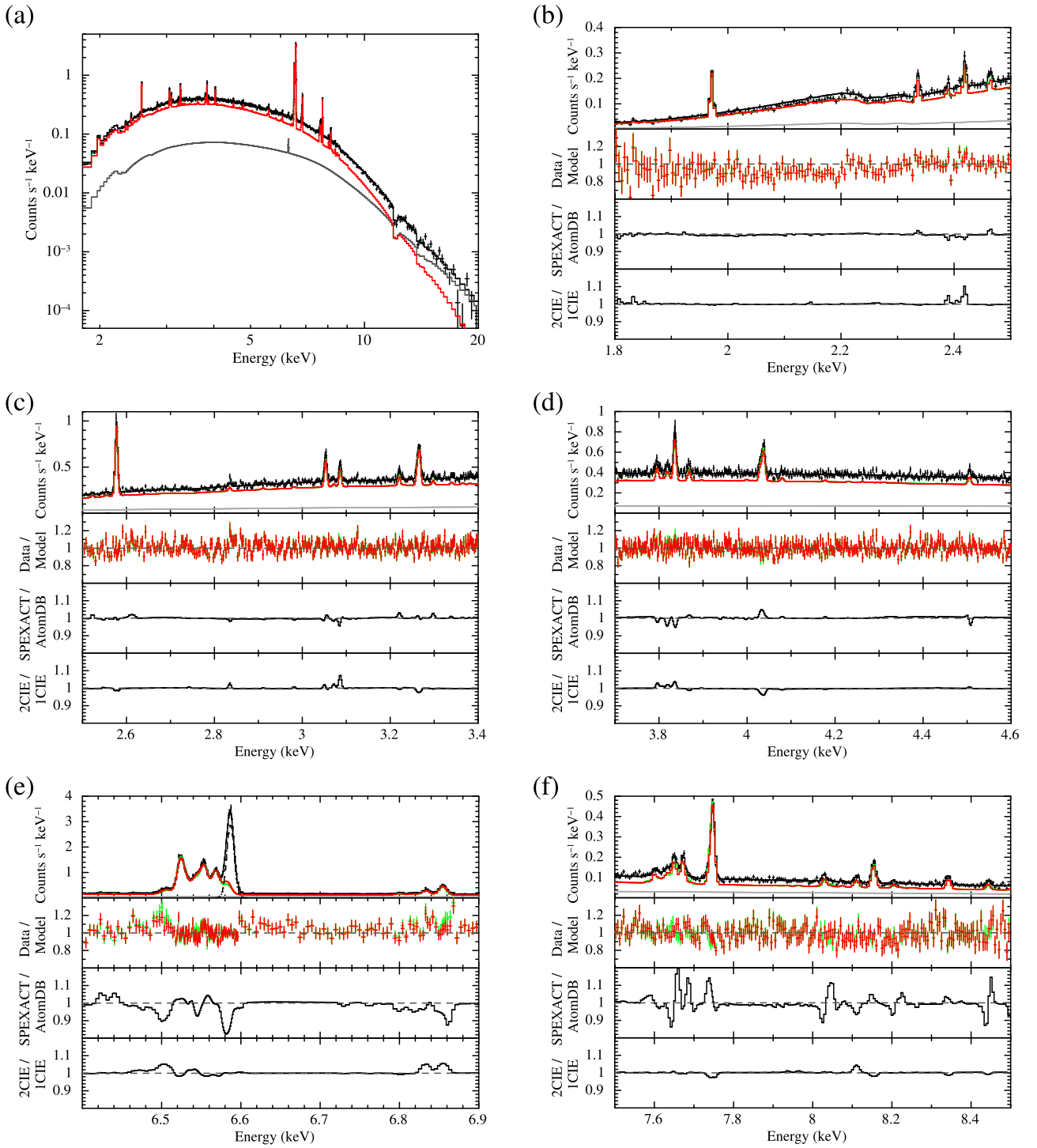
Fig. 6. Spectra in the Entire Core region fitted with the modified-1CIE model. The entire energy band of 1.8–20.0 keV is shown in (a), and narrower energy bands of 1.8–2.5 keV, 2.5–3.4 keV, 3.7–4.6 keV, 6.4–6.9 keV, and 7.5–8.5 keV are shown in panels (b)–(f). The black solid curve is the total model flux, and the red and gray curves indicate the ICM component based on AtomDB and the AGN component, respectively; panels (b)–(f) include the green lines, indicating the ICM component based on SPEXACT. The panel (e), covering the 6.4–6.9 keV band, also shows the Gaussian (black-dashed curve) which substitutes Fe XXV w in the plasma model. All the spectra are rebinned after the fitting just for display purposes. The second subpanels in (b)–(f) are the ratios of the data to the models of AtomDB (red) and SPEXACT (green). The third subpanels in (b)–(f) are comparisons of SPEXACT and AtomDB in the modified-1CIE model. The bottom subpanels in (b)–(f) show the ratio of the 2CIE model to the modified-1CIE model based on AtomDB.
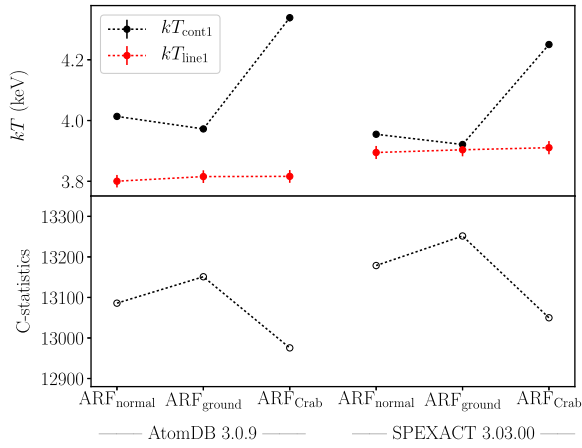
Fig. 7. Comparisons of the best-fit temperatures and C-statistics among different ARFs and different atomic databases for the modified-1CIE model. (Color online)

Fig. 8. Comparisons of the best-fit temperatures and C-statistics among different ARFs and different atomic databases for the 2CIE model. (Color online)

the resulting temperatures, the ratio of the normalizations (N_2/N_1), and the C-statistics for each ARF. The best-fit parameter values vary significantly, depending on the choice of ARF, but the temperatures of ARF_{normal} and ARF_{Crab} are very close to each other ($\sim$3 keV plus $\sim$5 keV). Only ARF_{ground} shows the presence of a >20 keV component, which seems physically less well motivated. The different trend in ARF_{ground} is likely caused by an incomplete modeling of the continuum; as shown in the middle panel of figure 16 (appendix 4), concave residuals are seen in the 2–7 keV band for ARF_{ground}. In any case, the trend where the dominant component has a temperature of 3–4 keV and the subdominant additional phase has a higher temperature is robust.

3.2.3 Other combinations of collisional plasma models
We also tried to add one more CIE component to the 2CIE model (i.e., 3CIE model), but no significant improvements of the C-statistics were found. Therefore, the 2CIE model is sufficient to reproduce the observed spectrum.

The actual temperature structure of the ICM might not consist of discrete temperature components, but rather of a continuous temperature distribution. Indeed, some hints of a power-law or a Gaussian temperature distributions were reported in the literature (e.g., Kaastra et al. 2004; Simionescu et al. 2009). We therefore applied these simple differential emission measure (DEM) models to the SXS spectrum. The emission measure profile, $EM(kT)$, is proportional to $(kT/kT_{max})^\alpha$ for the power-law DEM model and to $\exp[-(kT - kT_{mean})^2/2\sigma]$ for the Gaussian DEM model. The best-fit parameters of the models are summarized in table 4. Both the power-law DEM and the Gaussian DEM models show steep temperature distributions peaked at $\sim$4 keV, even though the distributions based on SPEXACT are slightly wider (smaller index or larger σ) than those
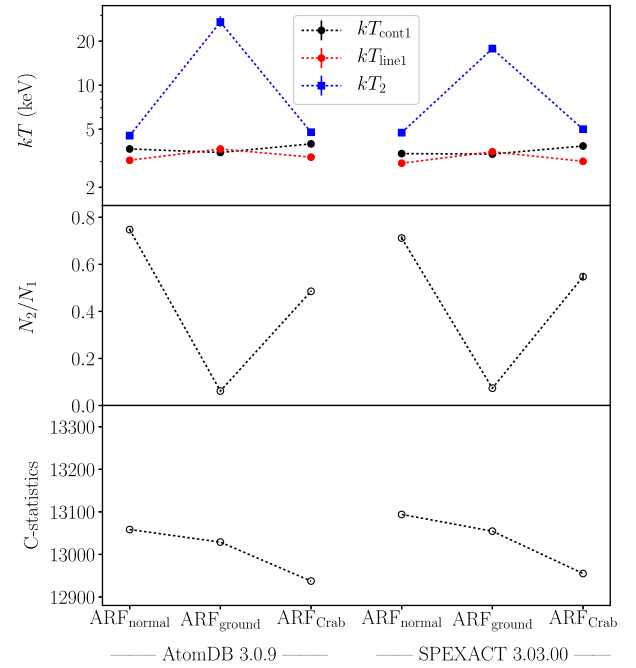
based on AtomDB. In any case, we found no significant improvements from the 2CIE model. A further investigation of the multi-temperature model is shown in subsection 3.4 and figure 10.

Another possible cause of the deviation from a single-temperature model shown in the line ratio diagnostics is the NEI state, which is often observed in supernova remnants. We thus tried to fit the spectrum with a NEI model (the possibilities of both an ionizing plasma and a recombining plasma are considered). However, the obtained ionization parameter becomes $nt > 1 \times 10^{12}\,\mathrm{cm}^{-3}\,\mathrm{s}^{-1}$, and the temperature is almost the same as the 1T model; therefore, the model is consistent with a CIE state, and we find no significant signature of the NEI.

3.3 Spatial variations of the temperature structure
We next modeled the broad-band spectra in the Nebula, Rim, and Outer regions in order to look for spatial trends in the temperature distribution. The fit results obtained with the modified-1CIE model are given in the top rows of table 5. Compared to the result from the Entire Core region, the temperature in the Nebula region is slightly lower, while that in the Rim region is slightly higher. The temperature continues to increase at larger radii, reaching 5 keV in the Outer region. These results are consistent with the temperature map obtained from XMM-Newton and

Table 5. Best fit parameters for the Neubla, Rim, and Outer regions.

Model/parameter	AtomDB v3.0.9			SPEXACT v3.03.00		
	Nebula	Rim	Outer	Nebula	Rim	Outer
Modified-1CIE model						
$kT_{\rm cont}$ (keV)	$3.96^{+0.01}_{-0.01}$	$4.02^{+0.01}_{-0.01}$	$4.93^{+0.10}_{-0.10}$	$3.90^{+0.02}_{-0.02}$	$3.97^{+0.01}_{-0.01}$	$4.85^{+0.09}_{-0.09}$
$kT_{\rm line}$ (keV)	$3.73^{+0.03}_{-0.03}$	$3.94^{+0.04}_{-0.04}$	$4.83^{+0.15}_{-0.16}$	$3.82^{+0.03}_{-0.07}$	$4.07^{+0.04}_{-0.04}$	$4.97^{+0.16}_{-0.14}$
N (10^{12} cm^{-5})	$14.75^{+0.05}_{-0.05}$	$15.31^{+0.04}_{-0.04}$	$5.22^{+0.10}_{-0.11}$	$14.68^{+0.08}_{-0.08}$	$15.23^{+0.04}_{-0.04}$	$5.21^{+0.09}_{-0.09}$
C-statistics/dof	11948.0/12200	10168.9/10300	6323.8/6929	12013.0/12200	10188.6/10300	6326.5/6929
2CIE model						
$kT_{\rm cont1}$ (keV)	$3.56^{+0.42}_{-0.07}$	$3.65^{+0.02}_{-0.02}$	...	$3.39^{+0.07}_{-0.09}$	$3.40^{+0.02}_{-0.02}$	...
$kT_{\rm line1}$ (keV)	$2.78^{+0.10}_{-0.37}$	$3.49^{+0.05}_{-0.05}$	...	$2.60^{+0.24}_{-0.23}$	$3.27^{+0.05}_{-0.05}$	...
kT_2 (keV)	$4.32^{+0.02}_{-0.36}$	$4.98^{+0.05}_{-0.05}$	...	$4.30^{+0.28}_{-0.16}$	$4.99^{+0.04}_{-0.03}$	...
N_1 (10^{12} cm^{-5})	$6.91^{+0.45}_{-3.40}$	$11.16^{+0.06}_{-0.06}$	...	$6.24^{+2.14}_{-2.21}$	$9.94^{+0.06}_{-0.06}$	...
N_2 (10^{12} cm^{-5})	$7.73^{+3.46}_{-0.45}$	$4.28^{+0.04}_{-0.04}$	...	$8.32^{+1.56}_{-1.97}$	$5.47^{+0.05}_{-0.05}$	...
C-statistics/dof	11926.0/12198	10163.2/10298	...	11958.2/12198	10173.3/10298	...
PSF-corrected model						
$kT_{\rm cont1}$ (keV)	$3.64^{+0.03}_{-0.03}$	$3.92^{+0.02}_{-0.02}$	$5.11^{+0.05}_{-0.05}$	$3.46^{+0.03}_{-0.03}$	$3.82^{+0.02}_{-0.02}$	$5.01^{+0.06}_{-0.05}$
$kT_{\rm line1}$ (keV)	$2.68^{+0.04}_{-0.05}$	$3.88^{+0.05}_{-0.05}$	$5.00^{+0.16}_{-0.16}$	$2.66^{+0.04}_{-0.04}$	$3.97^{+0.06}_{-0.05}$	$5.19^{+0.17}_{-0.16}$
kT_2 (keV)	$4.27^{+0.03}_{-0.03}$	$5.37^{+0.28}_{-0.30}$	...	$4.53^{+0.03}_{-0.03}$	$6.80^{+0.56}_{-0.46}$	...
N_1 (10^{12} cm^{-5})	$5.54^{+0.04}_{-0.04}$	$10.18^{+0.05}_{-0.05}$	$4.51^{+0.04}_{-0.04}$	$6.63^{+0.05}_{-0.21}$	$10.35^{+0.05}_{-0.05}$	$4.52^{+0.04}_{-0.04}$
N_2 (10^{12} cm^{-5})	$5.86^{+0.03}_{-0.04}$	$0.70^{+0.04}_{-0.03}$	...	$4.72^{+0.04}_{-0.04}$	$0.52^{+0.04}_{-0.03}$	...
C-statistics/dof		28404.6/29425			28444.1/29425	

Chandra observations (Churazov et al. 2003; Sanders & Fabian 2007).

The line-ratio diagnostics show a deviation from the single-temperature approximation in the Nebula and Rim regions. We thus applied the 2CIE model to the spectra of those regions. The best-fit parameters are also shown in the middle rows of table 5. The C-statistics were improved from the modified-1CIE model ($\Delta C = 6$–59). Both the Nebula and Rim regions show the same composition as the Entire Core region (roughly 3 keV plus 5 keV), but with different normalization ratios (the relative contribution of the hotter component is lower in the Rim region, although significant differences between the two spectral codes are also found). Large asymmetrical errors of the normalizations in the Nebula region are likely due to the comparable normalization values of the two components and the limited energy band (>1.8 keV). In the Nebula region, the discrepancy between $kT_{\rm cont}$ and $kT_{\rm line}$ becomes large (~ 1.0 keV), and $kT_{\rm line}$ shows the lowest temperature of ~ 2.7 keV among the different spatial regions considered. We also checked the 2CIE model in the Outer region, but no improvements from the modified-1CIE model were found ($\Delta C < 1$), as expected from the line-ratio diagnostics. The systematic uncertainty of the temperature measurements due to the different ARFs has a similar trend as the analysis of the Entire Core region (see appendix 4).

Table 6. Fraction of integrated photons coming from each sky region.

Integrated region	Sky regions		
	Nebula	Rim	Outer
Nebula	0.800	0.192	0.008
Rim	0.273	0.719	0.007
Outer	0.034	0.111	0.855

The sizes of the regions used for spatially resolved spectroscopy are comparable to the angular resolution of the telescope. Therefore, photons scattered from the adjacent regions due to the telescope's PSF tail might affect the fitting results. We calculated the expected fraction of scattered photons with ray-tracing simulations, and give the results in table 6: the fractions reach up to 30%, and are not negligible. We thus performed a "PSF-corrected" analysis, in which all the regions were simultaneously fitted taking into account the expected fluxes of photons scattered between regions. We used the 2CIE model for the Nebula and Rim regions and the 1 CIE model for the Outer region according to the results presented above. The best-fit parameters of the PSF-corrected model are given in the bottom rows of table 5. After the PSF correction, the ratios of the normalizations are changed, but the temperatures we obtained are almost
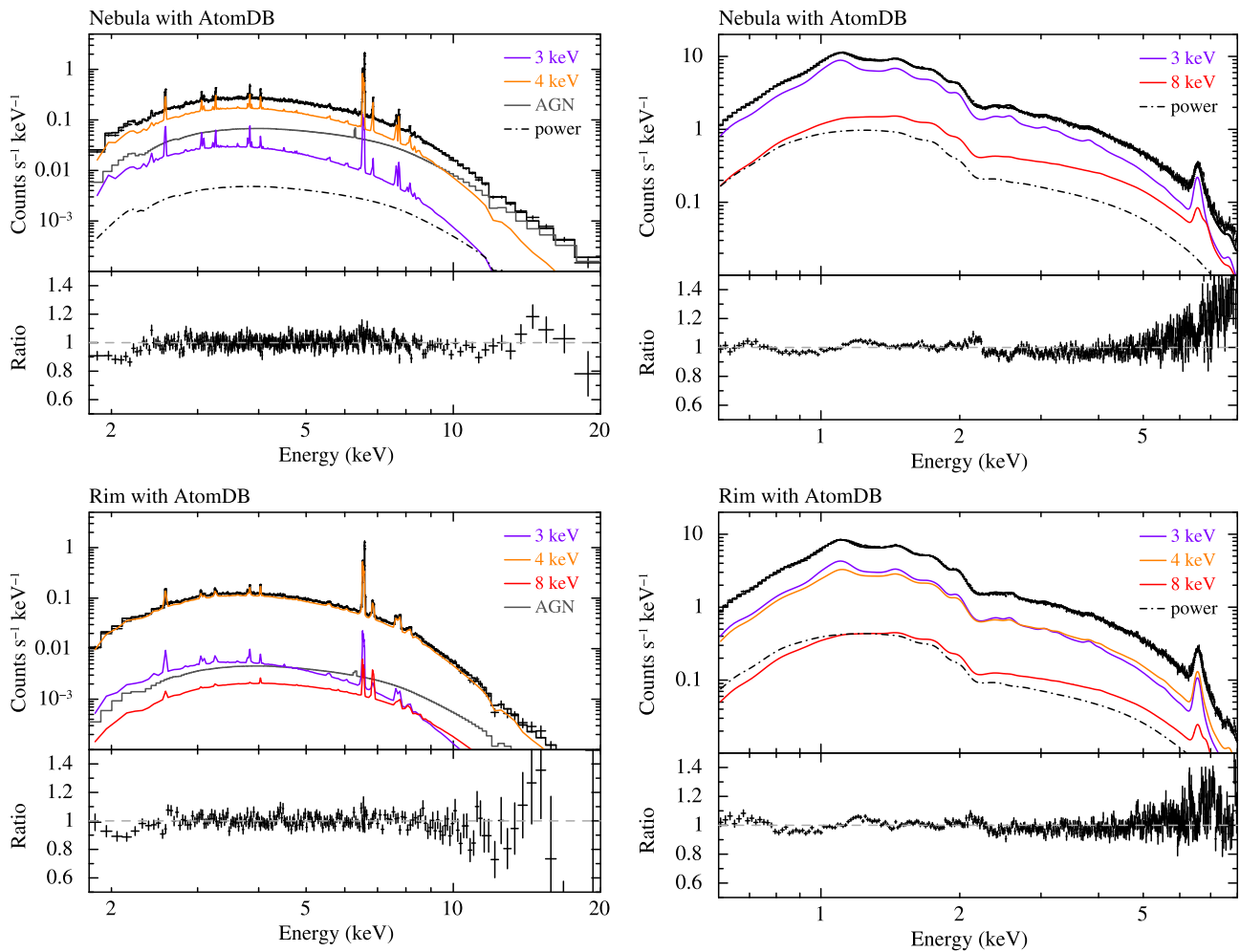
Fig. 9. Spectra fitted with the six-temperature model (upper panels) and ratios between the data and the model (lower panels). Left- and right-hand columns show the Hitomi/SXS and Chandra/ACIS spectra, respectively. The top and bottom rows correspond to the Nebula and Rim regions, respectively. The components included in the model are shown in color lines as denoted in each panel. The components whose normalizations are very low are not shown.

consistent with those derived from the PSF "uncorrected" analysis.

3.4 Comparison with multi-temperature models from previous observations

Chandra/ACIS and XMM-Newton/RGS observations revealed a multi-temperature structure ranging between 0.5–8.0 keV in the core of the Perseus cluster (Sanders & Fabian 2007; Pinto et al. 2016). Here we use a similar multi-temperature analysis to check the consistency between Hitomi/SXS and these previous measurements.

We fitted the SXS spectra extracted from the Nebula and Rim regions with a six-temperature CIE model consisting of 0.5 keV, 1 keV, 2 keV, 3 keV, 4 keV and 8 keV components following Sanders and Fabian (2007). The temperature of each component was fixed, and the abundance and line-of-sight velocity dispersion were common to all of the

components. The power-law component that was found in Sanders and Fabian (2007) and interpreted as a possible inverse-Compton emission was also included in our model with a fixed photon index of $\Gamma = 2$. The spectra and the best-fit models in the Nebula and Rim regions are shown in the left-hand column of figure 9. The normalizations we obtained for each temperature were scaled so as to sum to unity; the results are plotted in figure 10 as red diamonds. For the profile of the scaled normalizations there are high similarities between AtomDB and SPEXACT, except for the 8 keV component, which is detected with SPEXACT in both the Nebula region and the Rim region while only its upper limit was obtained for AtomDB. The results indicate that the combination of the 3 keV, 4 keV, and 8 keV components approximates the 2CIE model obtained in subsection 3.3 (roughly 3–4 keV plus 5 keV).

We also reanalyzed the Chandra/ACIS data because the effective area calibration was significantly improved during
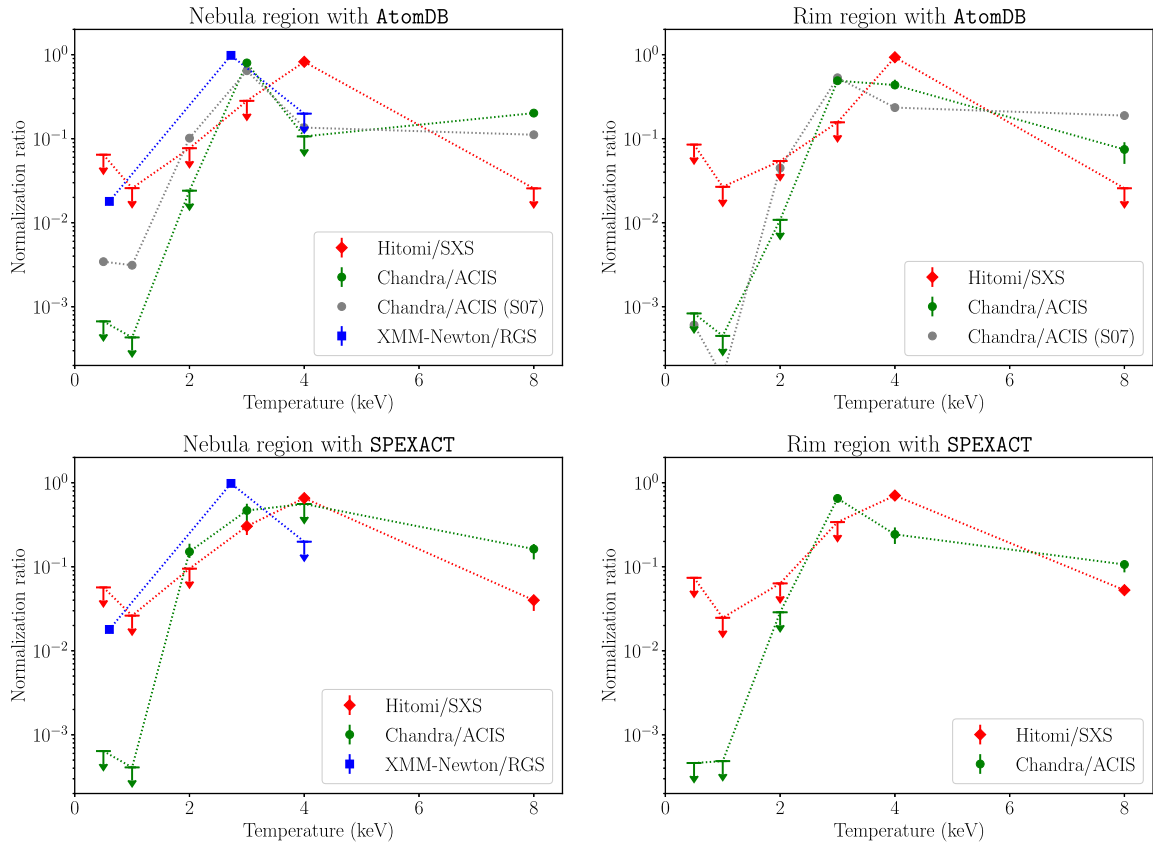
Fig. 10. Normalization ratios of each temperature component derived from the multi-temperature models. The top row is the results from `AtomdB` and the bottom row is those from `SPEXACT`. The left- and right-hand columns correspond to the Nebula and Rim regions, respectively. The red diamonds are Hitomi/SXS, the black circles are Chandra/ACIS, the gray circles are Chandra/ACIS of Sanders and Fabian (2007), and the blue squares are XMM-Newton/RGS. The results of XMM-Newton/RGS are shown only in the Nebula region because the RGS data does not cover the Rim region. (Color online)

2007–2009 (Nevalainen et al. 2010) and the atomic codes have been updated since the original work of Sanders and Fabian (2007). We fitted the spectra of the Nebula and Rim regions with the same six-temperature model as the SXS spectrum. The abundances and the velocity dispersion were fixed at the value obtained from the SXS analysis, because Chandra's energy resolution is not sufficient to determine these parameters. The AGN model was not included, because we excluded the AGN from the ACIS spectral extraction region. When the absorption column density was fixed at $1.38 \times 10^{21}\,\mathrm{cm}^{-2}$, we found a significant excess of the model over the data below 1 keV. We therefore allowed the absorption column density to vary to compensate for these residuals. The best-fit column density is $\sim 2.0 \times 10^{21}\,\mathrm{cm}^{-2}$ for both the Nebula and Rim regions. The fitting spectra are shown in the right-hand column of figure 9. Large residuals can be seen above 5 keV in the Nebula region. Fitting these residuals with an additional power-law would require this to have a negative photon index. Therefore, we suspect these residuals are due to an instrumental effect rather than true

astrophysical emission. The fact that no such residuals are seen in the SXS spectrum supports this inference. In addition, we see the wavy residuals in the entire energy band, which is probably due to the systematic uncertainty of the detector responses. The scaled normalizations we obtained are plotted in figure 10 as black circles. The two spectral codes show similar trends, except for the 2 keV component in the Nebula region that is seen with `SPEXACT` but not with `AtomDB`.

Compared to the results of Sanders and Fabian (2007), our ACIS analysis shows a similar trend, but ≤2 keV components are not detected (figure 10). That is probably because the analysis of Sanders and Fabian (2007) used much smaller regions, and could detect the lower-temperature component that is concentrated in the cluster core and the filamentary structures. In the spectra of our analysis, which is taken from a much larger region, the lower-temperature components could be smeared out by the dominant higher temperature component.

The Hitomi/SXS upper limits of the ≤2 keV components are consistent with the Chandra/ACIS results.
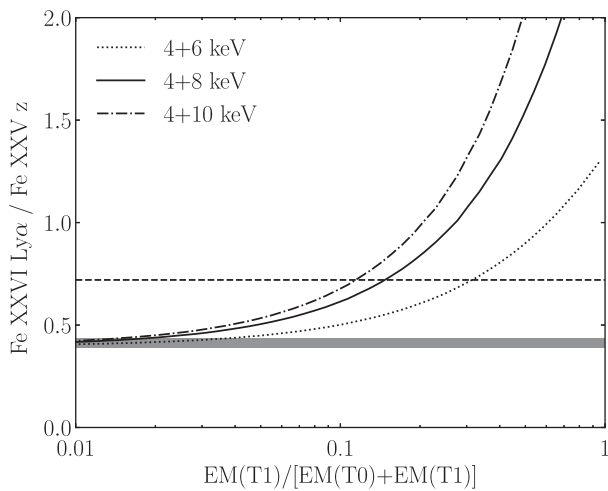
Fig. 11. Model line flux ratios of Fe XXVI Lyα to Fe XXV z as a function of the fractional emission measure of the secondary component in a two-CIE model based on `AtomDB`. The temperature of the main component (*T0*) is 4.0 keV. The solid, dotted, and dot-dashed lines show the models for a second component with a temperature (*T1*) of 8.0, 6.0, and 10.0 keV, respectively. The ratio of SXS measurement in the Nebula region (0.41 ± 0.02) is shown by the gray shading area, and that of the Chandra model in the same region (0.8) is shown by the horizontal dashed line.

However, the distribution of the higher temperature components seems to be somewhat different. The 4 keV component has the highest normalization in the SXS analysis, while the 3 keV component seems dominant in the ACIS fit. When the lower end of the energy band for the ACIS analysis was changed to 1.8 keV, just the SXS analysis, we found that the peak of the normalization ratio became 4 keV. This suggests that a derived normalization ratio of the ACIS analysis is affected by the fitting energy band, especially the band of Fe L-shell lines. The normalization of the 8 keV component for the SXS is lower than that for the ACIS by a factor of 2–10. To show the sensitivity of the line ratio, Fe XXVI Lyα/Fe XXV z, to the 8 keV component emission, we calculated the line ratio as a function of its fractional emission measure given in figure 11. The SXS observed line ratio (∼0.4) and the expected line ratio derived from the best-fit ACIS multi-temperature model is also shown in the same figure. This indicates that the line flux of Fe XXVI Lyα primarily limits the hotter component emission. This SXS spectroscopic constraint is more robust and less dependent on the modeling of the continuum components, compared with the previous continuum-based analysis.

Although we employed this particular six-temperature model just to examine the consistency with the Chandra result (Sanders & Fabian 2007, and our own analysis), we admit that the assumed six temperatures are not necessarily appropriate, because no emission measure is considered between the temperatures of 4 keV and 8 keV.

Table 7. Surface brightness of the power-law component.*

Instrument	AtomDB 3.0.9		SPEXACT 3.03.00	
	Nebula	Rim	Nebula	Rim
Hitomi/SXS	<3.4	<1.2	<1.8	<0.6
Chandra/ACIS	$6.3^{+0.5}_{-0.5}$	$2.0^{+0.3}_{-0.3}$	$6.6^{+0.5}_{-0.5}$	$1.9^{+0.3}_{-0.3}$

*In units of 10^{-16} erg cm^{-2} s^{-1} arcsec^{-2} (2–10 keV band).

This condition is inconsistent with the very likely presence of a component with ∼5 keV temperature in the present SXS spectra, as indicated in table 5 by the 2T fit to the Nebula and Rim spectra. In addition, the outer region of Perseus is known to have a typical temperature of 6–7 keV (e.g., Churazov et al. 2003), and such a component must contribute to the SXS spectra at least due to projection. Given these, we repeated the multi-temperature fitting by adding the 7th component with its temperature fixed at 6 keV. As a result, the Nebula spectrum constrained the normalization (the same as in figure 10) of this 6 keV component as <0.05 with `AtomDB` and <0.13 with `SPEXACT`, which are lower than those for the 4 keV emission. At the same time, the SXS normalization of the 8 keV component is <0.03 with `AtomDB` and <0.07 with `SPEXACT`, and is consistent with the six-temperature results. Therefore, the additional 6 keV component has no significant effect on the normalizations of the other temperature components.

The fluxes of the additional power-law component are given in table 7. The SXS detected no significant power-law component, while the ACIS data clearly require it in both the Nebula region and the Rim region. These differences are discussed in subsection 4.3.

The RGS data cover the energy band below 2 keV with high spectral resolution, and is complementary to the Hitomi/SXS data. Indeed, a very low temperature component with $kT < 1$ keV was reported from the XMM-Newton/RGS observations (Pinto et al. 2016). Here, we fitted the RGS spectrum with a three-temperature plasma model by adding a fixed-temperature 4 keV component to the two-temperature model used in Pinto et al. (2016). For the RGS analysis, we have used the SPEX fitting package, because accounting for the line broadening due to the spatial extent of the source is not easily implemented in Xspec. A `user` model which calls Xspec externally and which returns the model calculation to SPEX is used as an implement of fitting `AtomDB` to the RGS data.

The obtained best-fitting temperatures are $0.60^{+0.02}_{-0.02}$ keV and $2.7^{+0.08}_{-0.05}$ keV for `AtomDB` and $0.55^{+0.03}_{-0.06}$ keV and $2.4^{+0.08}_{-0.10}$ keV for `SPEXACT`. The relative normalizations of each component are over-plotted in figure 10. The profile peaks at $kT \sim 2.5$ keV, lower than both Chandra
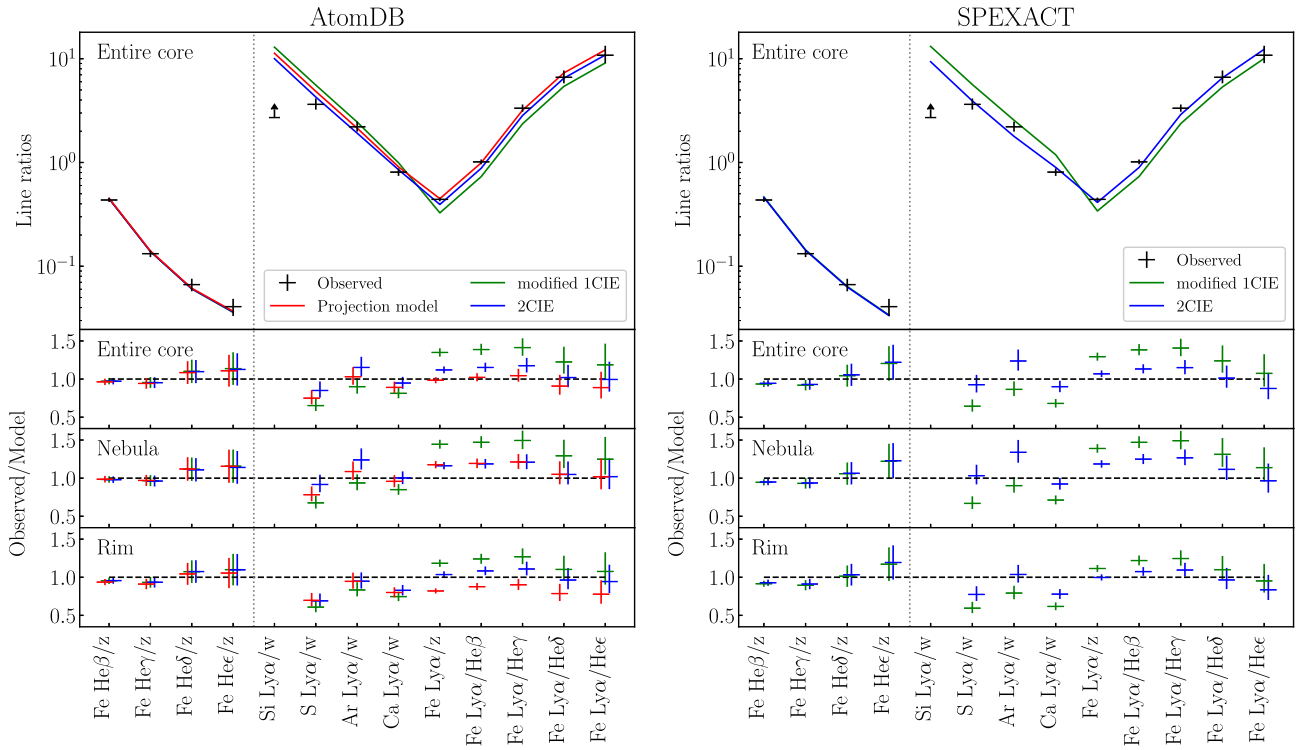
Fig. 12. Comparisons between the observed line ratios (black crosses), the modified-1CIE model (green line), the 2CIE model (blue line), and the projection model (red line). The left- and right-hand figures show the calculations based on AtomDB and SPEXACT, respectively. The projection model is not shown in the right-hand (SPEXACT) figure. The lower subpanels show the ratios of the observation to the model in the Entire Core, Nebula, and Rim regions from top through bottom. The vertical dotted line in the panels separates the ratios measuring the excitation temperature (left side) and the ionization temperature (right side).

and Hitomi, and gives a significant detection of gas with $kT \sim 0.6$ keV. The normalization of this low-temperature component measured with RGS is consistent with the Hitomi, but not with the Chandra upper limits for the 0.5 keV gas included in the six-temperature model: the upper limits for the 4 keV gas in both RGS and Chandra are lower than the Hitomi measurement for this temperature.

A simultaneous fitting of the SXS, ACIS, and RGS might provide a more complete picture of the temperature distribution. However, cross-instruments issues, such as the different spectral extraction regions and cross calibration of the effective areas, require more detailed analysis concerning the systematic errors. We therefore consider such an analysis as a future work.

4 Discussion

4.1 Origin of the deviations from a single-temperature model

The line-ratio diagnostics presented in subsection 3.1 show that, with the exception of the Outer region, the derived ionization temperatures are different for each element (figure 5), and indicate a multi-temperature structure.

In subsection 3.2, we modeled the spectrum of the Entire Core, Nebula, and Rim regions with single- and two-temperature plasma models. In figure 12, we compare the observed line ratios and the line ratios predicted by the modified-1CIE and the 2CIE models, in order to investigate how these model approximations are capable of reproducing the observations, and where the biggest discrepancies are found. This figure includes not only the line ratios that allow us to estimate the ionization temperatures, but also those sensitive to the excitation temperatures (Fe Heβ/z, Heγ/z, Heδ/z, and Heϵ/z). As expected from the C-statistics shown in tables 4 and 5, the line ratios of the 2CIE models are closer to the observed ones than those of the modified-1CIE models in all the region and in both AtomDB and SPEXACT. We then calculated chi-squared values (χ^2) of the 2CIE models with respect to the observed line ratios in the Entire Core region. The results are 22.0 and 19.6 in AtomDB and SPEXACT, respectively, for 12 considered line-ratio measurements. The major line ratios are reproduced better by the 2CIE model of SPEXACT, even though the broad-band fitting with the 2CIE model gives larger C-statistics in SPEXACT than AtomDB (table 4).

One of the physical origins of the multi-temperature structure is the projection effect: the radial temperature

gradient from the core to the outskirts is accumulated along the line of sight. In order to check this possibility, we used the azimuthally averaged radial profiles of the temperature, density, and abundances derived from the de-projection analysis of the Chandra data using `AtomDB` (see figure 7 in the RS paper). In this radial profile model, the temperatures vary from 3 keV to 6.5 keV with increasing radius from the cluster center in the range of 3–1000 kpc. We integrated this model along the line of sight and calculated the model line ratios shown in red in figure 12 (left). The projection model of `SPEXACT` is not shown because the radial profile is derived based on `AtomDB`. In the Entire Core region, χ^2 of the projection model is 13.0, and is considerably better than that of the 2CIE model ($\chi^2 = 22.0$). On the other hand, in the Nebula and Rim regions, the projection model is almost the same or even worse, compared to the 2CIE model. Azimuthal variation in temperature is probably significant in the Nebula and Rim regions, as observed with Chandra (e.g., Fabian et al. 2011), and this likely causes a difference between the azimuthal variation and the projection model that is based on the azimuthally averaged radial profile.

A configuration in which the two-temperature components determined from the 2CIE model are truly co-spatial cannot be ruled out. However, the derived temperatures in the 2CIE model ($\sim$3 keV plus $\sim$5 keV) are very close to the temperatures observed in the cluster center and outer region. Therefore, the projection effect naturally explains the observed trend of lower ionization temperatures for ions with lower atomic numbers. Since the equivalent widths of spectral lines from lighter elements are generally larger for lower temperatures, in the presence of a radial gradient along the line of sight, the emission-measure weighted average fluxes of these lines will naturally be biased toward the cooler gas, while the emission-measure weighted average fluxes of elements with higher atomic numbers will be biased toward values being more typical of the hotter gas.

The low-temperature gas components ($kT < 3$ keV) reported in previous Chandra and XMM-Newton observations are not seen in figure 12. That is simply because the Hitomi/SXS energy band is restricted to energies above 1.8 keV, and so is not sensitive to such low-temperature components; accordingly, the upper limits derived from Hitomi for these thermal phases are not in conflict with previous results.

4.2 Uncertainties in modeling the multi-temperature plasma

In subsection 3.4, we compared the Hitomi/SXS results with the Chandra/ACIS and the XMM-Newton/RGS results. The best-fit emission measure distribution as a function of temperature is different among instruments (figure 10): the normalization peaks at temperatures of 4 keV, 3 keV, and 2 keV for the SXS, ACIS, and RGS, respectively. The uncertainty of the detector response also affects the results, as shown by the discrepancy of the 8 keV component in the Hitomi/SXS and Chandra/ACIS.

Even in the single- or two-temperature model, the best-fit parameters are sensitive to the effective area calibration as demonstrated in figure 7, figure 8, and appendix 4. In the single-temperature modeling, we can robustly determine temperatures using only the line fluxes. However, in the two-temperature modeling, it is difficult to determine both temperatures and normalizations exactly.

Furthermore, we found that a small change in the atomic code significantly affects the result. As shown in appendix 6, the `AtomDB` 3.0.8 gives temperatures of 1.7 keV and 4.1 keV in the 2CIE model, which are completely different from the results based on `AtomDB` 3.0.9. The difference between the two codes is only the emissivity of the dielectric-recombination satellite lines that is significantly lower than that of the transitions in the He-like ions (w, x, y, and z).

Therefore, we demonstrated that quantifying deviations from a single-temperature model is a complex problem. As shown in figure 6, the spectral differences between a two-temperature model consisting of a mixture of 3 and 5 keV plasma and a single-temperature model with $kT = 4$ keV are very small, and thus the results of the 2CIE fit are sensitive to a large number of factors. These factors include the analysis energy band, the energy resolution, the calibration of the effective area, and atomic codes. For an accurate analysis of the multi-temperature, non-dispersive high-resolution spectroscopy, a broad spectral band (0.5–10 keV), as will be achieved by XARM and Athena, is necessary.

4.3 Upper limit for the power-law component

The diffuse radio emission is thought to be generated by synchrotron mechanism of relativistic energy electrons with a 0.1–10 μG magnetic field in the ICM (Brunetti & Jones 2014). These electrons scatter the CMB photons via the inverse-Compton scattering, which allows us to investigate the magnetic field in the ICM (Ota 2012). Based on an assumption that inverse-Compton emission is generated by the same population of relativistic electrons, the volume-integrated magnetic field strength can be derived from intensities/upper-limits of IC emission (Rybicki & Lightman 1979).

Sanders and Fabian (2007) reported on the detection of a diffuse power-law component in the core of the Perseus cluster, which was not confirmed by the

XMM-Newton analysis (Molendi & Gastaldello 2009). The corresponding surface brightness in the 2–10 keV band measured by Sanders and Fabian (2007) is $\sim 15 \times 10^{-16}$ and $\sim 8 \times 10^{-16}$ erg cm^{-2} s^{-1} arcsec^{-2} in the Nebula and Rim regions, respectively. Our reanalysis of the Chandra/ACIS data also suggests the presence of such a power-law component, but with observed fluxes lower by a factor of 2–4 in better agreement with the upper limit of 5×10^{-16} erg cm^{-2} s^{-1} arcsec^{-2} reported by Molendi and Gastaldello (2009). That is likely caused by the update of the calibration database described in Nevalainen, David, and Guainazzi (2010); the response for the higher energy band is improved and significantly reduces the flux in that energy band.

In contrast, the Hitomi/SXS results show upper limits for this power-law component that are significantly lower than the fluxes measured with Chandra/ACIS. As shown in figure 9, large systematic residuals are present above 5 keV in the Chandra spectra even after the update of the effective area calibration, and they likely bias the power-law fluxes. A similar discrepancy was also reported in comparison with the XMM-Newton/EPIC results (Molendi & Gastaldello 2009). Since the Hitomi/SXS covers a wider energy range up to 20 keV, the obtained upper limits would be robust at least in the Rim region, in which the level of the AGN contamination is low.

Assuming that the power-law component is due to inverse-Compton scattering, we can estimate the strength of the magnetic field (B) as discussed in Sanders, Fabian, and Dunn (2005). Using the SXS upper limit of $<1.2 \times 10^{-16}$ erg cm^{-2} s^{-1} arcsec^{-2} in the Rim region, we obtained a lower limit of $B > 0.4\,\mu$G. This value is consistent with the results of other observations performed at other wavelengths (~ 7–$25\,\mu$G) as discussed in Molendi and Gastaldello (2009).

5 Conclusion

Compared to the intricate structures revealed by the deep Chandra image of the core of the Perseus cluster (e.g., Fabian et al. 2011), at the first glance the high-quality Hitomi SXS spectra of this source, which are sensitive to the temperature range of $\gtrsim 3$ keV, present a surprisingly quiescent view: the velocity dispersions are rather small (First paper; V paper), the chemical composition is remarkably similar to the solar neighborhood (Z paper), and the spectra in the range of 1.8–20 keV are largely well approximated by a single-temperature model. The diffuse power-law component found by previous Chandra measurements is also not required by the Hitomi data.

We have resolved line emission from various ions. This provides the first direct measurements of the electron temperature and the ionization degree separately, from different transitions of He-like and H-like ions of Si, S, Ar, Ca, and Fe. Compared with previous temperature measurements mostly based on the continuum shape, the new diagnostics are more sensitive to excitation processes and plasma conditions. We found that all observed ratios are broadly consistent with the CIE approximation. However, there are two signs of slight deviation from a single-temperature model. First, there is a trend of increasing ionization temperature with atomic mass, particularly in the Nebula (central) region, and possibly also in the surrounding Rim region. Secondly, the excitation temperature from Fe (~ 3 keV) is lower than the corresponding ionization temperature and lower than the electron temperature determined from the spectral continuum (~ 4 keV) for the Nebula. In the Nebula and Rim regions, the best-fit two-temperature models suggest a mix of roughly 3 and 5 keV plasma, both of which are expected to be present based on deprojected temperature profiles previously measured with Chandra. On the other hand, the Outer region, corresponding to the farthest observation from the cluster core performed by Hitomi, shows no significant deviation from single temperature. No additional third-temperature component, Gaussian nor power-law DEM model, nor significant emission from NEI plasma is required to describe the spectra.

Even though we cannot rule out a true multi-phase structure in which different temperature components are co-spatial, the projection effect is a reasonable explanation for the observed deviations from a single temperature.

Best-fit models of lower-resolution spectra that include the energy band below 2 keV and the RGS spectra seem to present a contrasting picture, requiring a multi-phase thermal structure to which Hitomi observations are currently not sensitive to. It is clear that the dominant thermal component in the spectral fit depends on the energy band observed, and that detectors capable of covering simultaneously the emission lines from all phases of the ICM are needed in order to pin down the reliable temperature structure. High-resolution, non-dispersive spectroscopy with XARM or Athena will thus be crucial in order to assess the origin and robustness of the multi-temperature structure reported by CCD studies, and to verify to what extent the complexity of cluster cores revealed by high-spatial resolution images corresponds to an equally complex picture along the energy axis.

Author contributions

S. Nakashima led this study in data analysis and wrote the manuscript. K. Matsushita, A. Simionescu, and T. Tamura reviewed the manuscript fully. K. Sato and T. Tamura

performed a cross-check of the Hitomi/SXS analysis. Y. Kato analyzed the Chandra/ACIS archival data. A. Simionescu and N. Werner performed the XMM-Newton/RGS analysis. M. Furukawa and K. Sato constructed the projection model and checked the effect of the resonance scattering. M. Bautz, H. Akamatsu, M. Tsujimoto, H. Yamaguchi, K. Makishima, C. Pinto, Y. Fukazawa, R. Mushotzky, and J. de Plaa provided valuable comments that improved the draft. S. Nakashima, K. Sato, K. Nakazawa, T. Okajima, and N. Yamasaki contributed to fabrication of the instruments and performed the in-orbit operation and calibration.

Appendix 1. Gain correction

We checked the uncertainties of the gain scale of the SXS, and corrected them using the Perseus data, themselves, because the gain scale calibration is limited due to the short life of Hitomi. The procedure described in this section is essentially the same as that used in the Z paper and Atomic paper, except that the reference redshift was changed from 0.01756 to 0.017284 according to the V paper.

We first applied a linear gain shift for each pixel in each observation so that the apparent energies of the Fe XXV lines agree with a redshift of 0.017284. The resulting amount of the energy shift at 6.5 keV is 1.0 ± 1.9 eV (mean and standard deviation). This pixel-by-pixel redshift correction removes not only the remaining gain errors among pixels, but also the spatial variation of the Doppler shift for the ICM. Our results are not affected by this possible "over-correction."

We then co-added spectra of all the pixels for each observation, and investigated the energy shifts of each line in
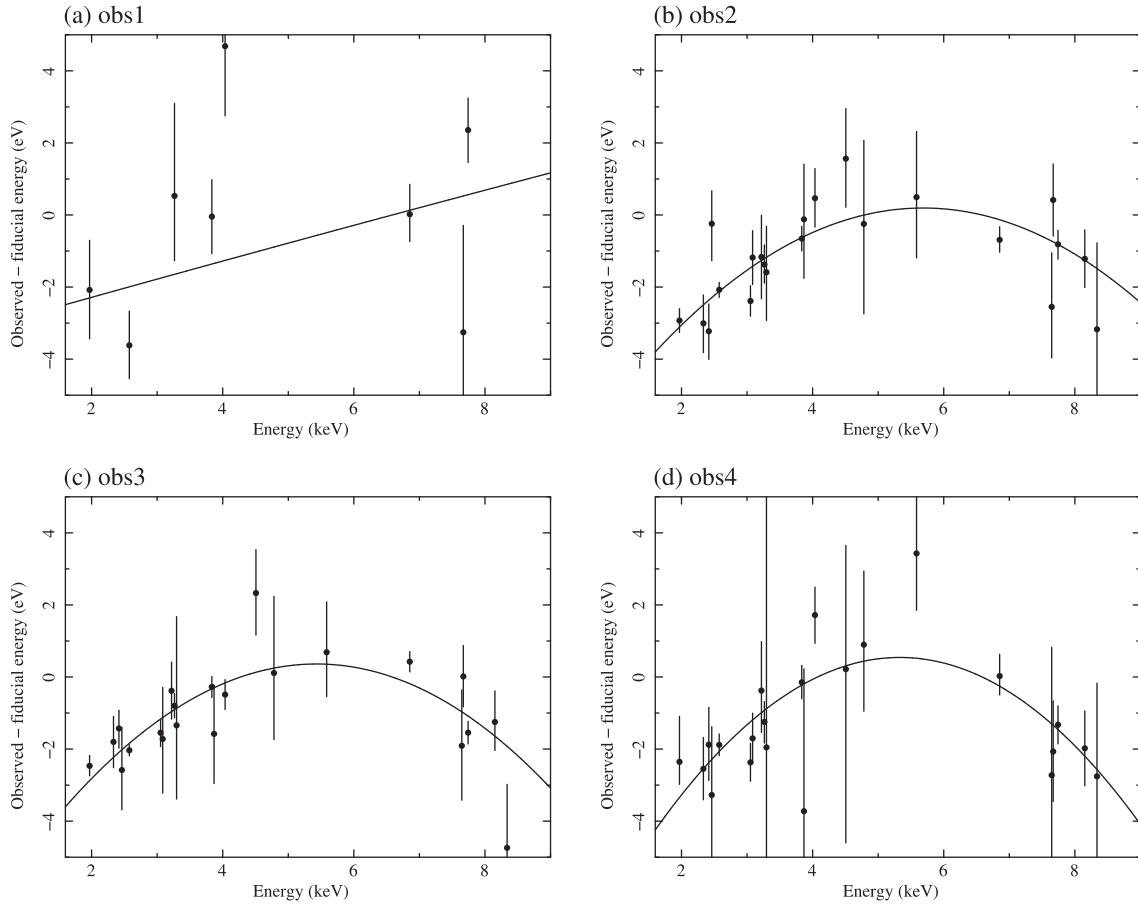
Fig. 13. Parabolic functions for the gain correction in each observation.

the 1.8–9.0 keV band. Figure 13 summarizes the differences between observed line energies and fiducial values assuming a redshift of 0.017284. We modeled these data by the parabolic function shown below, in which ΔE at $E = 6586.5$ eV was constrained to zero:

$$E_{\rm cor} = E + a \times (E - 6586.5) + b \times (E - 6586.5)^2 \ \text{eV}.$$
(A1)

The obtained parameters are as follows:

$$a = -4.888 \times 10^{-4} \quad \text{and} \quad b = 2.035 \times 10^{-6}, \quad (A2)$$

$$a = 4.303 \times 10^{-4} \quad \text{and} \quad b = 2.390 \times 10^{-4}, \quad (A3)$$

$$a = 6.250 \times 10^{-4} \quad \text{and} \quad b = 2.702 \times 10^{-4}, \quad (A4)$$

$$a = 8.640 \times 10^{-4} \quad \text{and} \quad b = 3.439 \times 10^{-4}, \quad (A5)$$

for obs1, obs2, obs3, and obs4, respectively. We applied these corrections to all of the pixels. As confirmed in figure 6 of the RS paper, these gain corrections have no impact on the line flux measurement, which is crucial for the temperature measurements.

Appendix 2. Detailed best-fit parameters of the Gaussian fits

The centers and widths derived from the Gaussian fits in subsection 3.1 are given in table 8. The obtained line widths are consistent with the results described in the V paper.

## Appendix 3. Single-line based on emission measure limits

In figure 14, we show theoretical emissivities for some of observed line transitions as a function of electron temperature based on AtomDB. The peak temperature from these ions, where the emissivity becomes maximum, covers a temperature range from 1.5 keV (H-like Si) to 13 keV (H-like Fe). Therefore, measurements of the line fluxes and ratios are sensitive to emission from plasma at around this temperature range.

Table 8. Observed line centers and widths derived from the Gaussian fits.*

Line name	E_0 (eV)[†]	Center (eV)				Width (eV)			
		Entire Core	Nebula	Rim	Outer	Entire Core	Nebula	Rim	Outer
Si XIII w	1865.0	$1864.5^{+1.1}_{-1.0}$	$1864.3^{+1.9}_{-0.9}$	(fixed)	(fixed)	<1.7	<1.7	(tied)	(tied)
Si XIV Lyα_1	2006.1	$2006.4^{+0.3}_{-0.2}$	$2006.5^{+0.3}_{-0.2}$	$2006.4^{+0.4}_{-0.3}$	$2006.5^{+1.2}_{-1.3}$	$1.4^{+0.3}_{-0.5}$	<1.5	$1.7^{+0.5}_{-0.5}$	<2.9
Si XIV Lyβ_1	2376.6	$2376.5^{+0.5}_{-0.5}$	$2376.2^{+0.5}_{-0.5}$	$2377.8^{+1.3}_{-1.4}$	$2378.5^{+1.1}_{-1.3}$	$2.4^{+0.5}_{-0.5}$	$2.2^{+0.5}_{-0.5}$	$3.8^{+1.3}_{-1.2}$	<2.0
S XV w	2460.6	$2460.7^{+0.5}_{-0.3}$	$2460.6^{+0.6}_{-0.4}$	$2460.7^{+0.6}_{-0.6}$	(fixed)	$2.2^{+0.6}_{-0.6}$	$2.6^{+0.8}_{-0.7}$	<2.2	(tied)
S XVI Lyα_1	2622.7	$2622.6^{+0.1}_{-0.1}$	$2622.7^{+0.1}_{-0.2}$	$2622.6^{+0.2}_{-0.2}$	$2621.6^{+0.9}_{-0.9}$	$1.8^{+0.2}_{-0.2}$	$1.9^{+0.2}_{-0.2}$	$1.7^{+0.3}_{-0.3}$	$2.0^{+1.0}_{-1.2}$
S XVI Lyβ_1	3106.7	$3106.4^{+0.3}_{-0.3}$	$3106.0^{+0.4}_{-0.4}$	$3107.0^{+0.3}_{-0.5}$	$3116.1^{+0.7}_{-1.3}$	$2.1^{+0.4}_{-0.3}$	$2.4^{+0.5}_{-0.4}$	$1.8^{+0.5}_{-0.7}$	<1.8
S XVI Lyγ_1	3276.3	$3276.8^{+0.8}_{-0.8}$	$3276.7^{+0.5}_{-0.8}$	$3276.3^{+1.0}_{-0.8}$	$3275.7^{+1.4}_{-1.4}$	<2.0	<2.1	$1.8^{+1.2}_{-1.4}$	<2.4
Ar XVII w	3139.6	$3139.5^{+0.3}_{-0.3}$	$3139.5^{+0.3}_{-0.4}$	$3139.3^{+1.2}_{-1.1}$	$3142.4^{+0.8}_{-1.0}$	$1.5^{+0.4}_{-0.4}$	$1.1^{+0.5}_{-0.6}$	$3.0^{+1.4}_{-1.1}$	<1.9
Ar XVIII Lyα_1	3323.0	$3322.9^{+0.2}_{-0.3}$	$3323.1^{+0.3}_{-0.4}$	$3322.5^{+0.5}_{-0.4}$	$3326.6^{+2.2}_{-2.2}$	$2.7^{+0.4}_{-0.4}$	$3.0^{+0.4}_{-0.4}$	$2.2^{+0.6}_{-0.6}$	$4.1^{+2.3}_{-1.6}$
Ar XVIII Lyβ_1	3935.7	$3935.0^{+0.9}_{-1.0}$	$3936.2^{+0.7}_{-1.3}$	$3931.4^{+1.5}_{-1.7}$	$3946.7^{+0.6}_{-1.2}$	$2.8^{+1.0}_{-0.8}$	$2.3^{+1.0}_{-0.9}$	$3.7^{+1.7}_{-1.6}$	<1.2
Ca XIX w	3902.4	$3902.4^{+0.2}_{-0.2}$	$3902.5^{+0.2}_{-0.3}$	$3902.1^{+0.3}_{-0.4}$	$3902.4^{+1.5}_{-1.1}$	$2.3^{+0.2}_{-0.2}$	$2.4^{+0.3}_{-0.3}$	$2.2^{+0.4}_{-0.4}$	$2.7^{+1.5}_{-1.2}$
Ca XIX Heβ_1	4583.5	$4583.9^{+0.4}_{-0.9}$	$4583.8^{+0.2}_{-0.9}$	(fixed)	(fixed)	<1.6	<1.4	(tied)	(tied)
Ca XX Lyα_1	4107.5	$4107.9^{+0.3}_{-0.5}$	$4107.1^{+0.7}_{-0.4}$	$4108.4^{+0.5}_{-0.6}$	$4113.1^{+1.8}_{-1.5}$	$2.6^{+0.4}_{-0.4}$	$2.9^{+0.5}_{-0.5}$	$2.4^{+0.7}_{-0.6}$	$3.0^{+2.1}_{-1.2}$
Fe XXV w	6700.4	$6700.7^{+0.0}_{-0.1}$	$6700.7^{+0.1}_{-0.1}$	$6700.6^{+0.1}_{-0.1}$	$6701.9^{+0.4}_{-0.2}$	$4.2^{+0.1}_{-0.1}$	$4.3^{+0.1}_{-0.1}$	$4.0^{+0.1}_{-0.1}$	$4.3^{+0.2}_{-0.2}$
Fe XXV z	6636.6	$6636.5^{+0.1}_{-0.1}$	$6636.4^{+0.2}_{-0.1}$	$6636.5^{+0.1}_{-0.2}$	$6637.5^{+0.5}_{-0.5}$	$3.4^{+0.1}_{-0.1}$	$3.6^{+0.1}_{-0.1}$	$3.2^{+0.2}_{-0.2}$	$3.9^{+0.5}_{-0.5}$
Fe XXV Heβ_1	7881.5	$7881.1^{+0.2}_{-0.2}$	$7881.3^{+0.3}_{-0.3}$	$7881.0^{+0.3}_{-0.3}$	$7882.6^{+0.5}_{-1.8}$	$4.2^{+0.2}_{-0.3}$	$3.8^{+0.3}_{-0.4}$	$4.4^{+0.3}_{-0.3}$	$5.0^{+0.9}_{-0.8}$
Fe XXV Heβ_2	7872.0	(tied)	(tied)	(tied)	(tied)	(tied)	(tied)	(tied)	(tied)
Fe XXV Heγ_1	8295.5	$8295.3^{+0.4}_{-0.6}$	$8295.5^{+0.7}_{-0.7}$	$8295.1^{+0.6}_{-1.1}$	(fixed)	$5.0^{+0.5}_{-0.5}$	$4.6^{+0.7}_{-0.6}$	$5.6^{+0.8}_{-0.7}$	<0.0
Fe XXV Heδ_1	8487.4	$8484.9^{+1.4}_{-1.2}$	$8485.7^{+1.7}_{-1.7}$	$8483.1^{+2.1}_{-1.7}$	(fixed)	$6.7^{+1.3}_{-1.0}$	$6.5^{+1.7}_{-1.3}$	$7.1^{+2.8}_{-1.6}$	<0.0
Fe XXV Heϵ_1	8588.5	$8592.6^{+1.3}_{-1.4}$	$8592.6^{+1.0}_{-1.9}$	$8594.3^{+1.4}_{-3.0}$	(fixed)	$4.8^{+1.2}_{-1.0}$	$3.8^{+1.4}_{-1.2}$	$7.8^{+3.5}_{-2.2}$	<0.0
Fe XXVI Lyα_1	6973.1	$6973.6^{+0.1}_{-0.5}$	$6973.3^{+0.4}_{-0.4}$	$6973.6^{+0.2}_{-0.6}$	$6973.9^{+1.1}_{-1.6}$	$4.3^{+0.2}_{-0.2}$	$4.7^{+0.3}_{-0.3}$	$3.8^{+0.2}_{-0.4}$	$6.1^{+1.2}_{-0.9}$
Fe XXVI Lyα_2	6951.9	$6952.8^{+0.3}_{-0.5}$	$6952.7^{+0.5}_{-0.8}$	$6952.6^{+0.5}_{-0.5}$	$6953.1^{+1.4}_{-1.9}$	(tied)	(tied)	(tied)	(tied)
Fe XXVI Lyβ_1	8252.6	$8255.3^{+1.0}_{-1.3}$	$8254.6^{+1.5}_{-0.5}$	$8254.7^{+1.5}_{-1.9}$	$8247.3^{+2.8}_{-0.9}$	<3.6	$3.0^{+2.2}_{-1.9}$	<1.6	<3.5
Ni XXVII w	7805.6	$7806.9^{+0.9}_{-0.6}$	$7807.2^{+0.9}_{-0.8}$	$7806.2^{+1.5}_{-1.2}$	$7804.0^{+2.5}_{-4.1}$	$5.4^{+0.8}_{-0.7}$	$5.4^{+0.9}_{-0.8}$	$5.8^{+1.7}_{-1.4}$	$6.6^{+3.6}_{-2.3}$

*The Lyα_2 lines of Si, S, Ar, and Ca are not shown because all the paramters of them are tied to Lyα_1 (see table 2 for details).

[†] Fiducial energies of the lines at the rest frame.
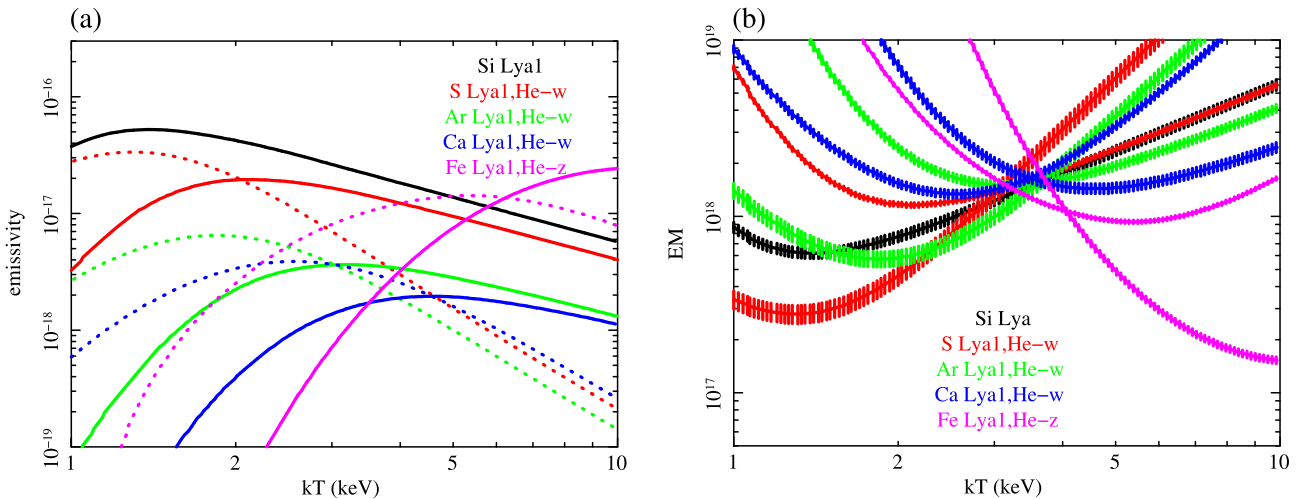
Fig. 14. (a) Line emissivities of strong transitions from `AtomDB` for a given emission measure and metal abundances. The solid and dashed lines show H-like and He-like transitions, respectively. (b) Emission measure limits calculated from the `AtomDB-CIE` model and the observed fluxes from the Entire Core region. (Color online)
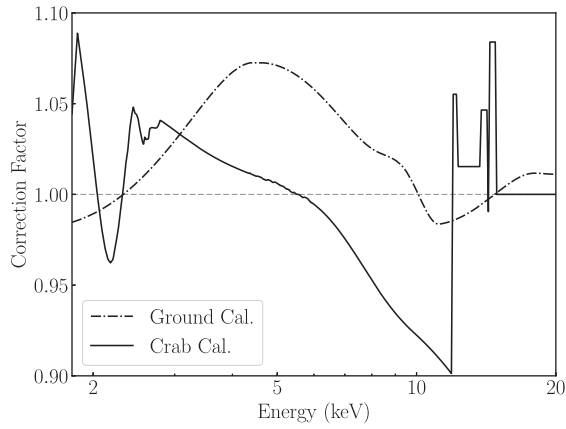
Fig. 15. Correction factors of the effective area with respect to the nominal value. The dot-dashed and solid lines indicate the calibrations with the ground data and with the actual Crab data, respectively.
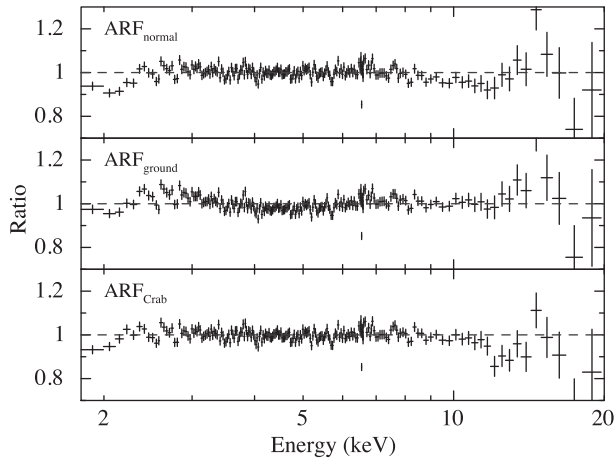
Fig. 16. Ratios of the Entire Core region spectrum to the best-fit modified-1CIE models with ARF$_{normal}$ (top), ARF$_{ground}$ (middle), and ARF$_{Crab}$ (bottom).

Combined with these emissivity values, the observed flux for each transition (table 3) provides constrains on emission measure for a given temperature and a metal abundance, as shown in figure 14. If the line emission originates from a single component CIE plasma, any two curves from a single element cross at a single point of the model temperature and emission measure. Furthermore, if the assumed metal abundances are correct, curves from different elements also cross at a single point. Our measured profiles from the Entire Core region intersect together at around 3–4 keV, indicating that the observed line fluxes, and hence their ratios, can be approximated by a single-component CIE plasma with the solar abundance ratios. From these curves we notice that the Fe XXVI Lyα is the most sensitive to hotter (>4 keV) emission and He-like S and He-like Ar lines are the most sensitive to cooler (<3 keV) emission.
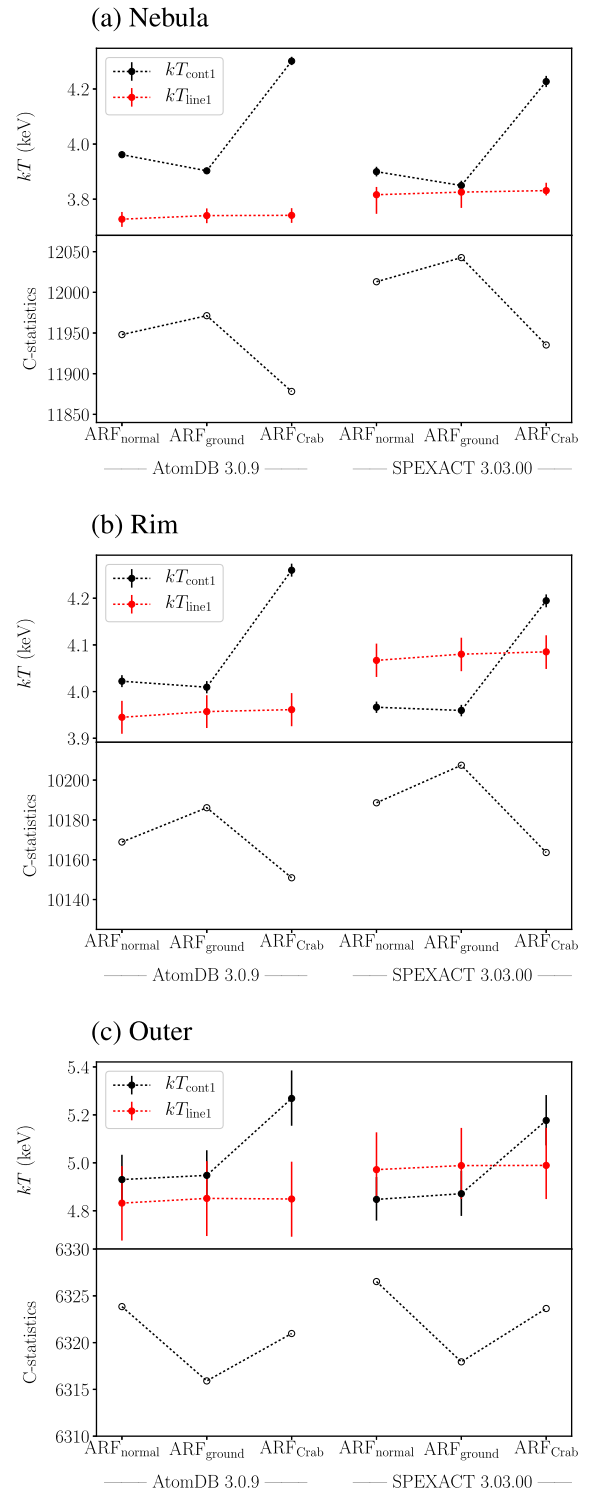
Fig. 17. Fitting results of the modified-1CIE model with different ARFs in the Nebula, Rim, and Outer regions. (Color online)

Appendix 4. Effective area uncertainties

Because of the short lifetime of Hitomi, its in-flight calibration plan is not completed. Data for the effective area
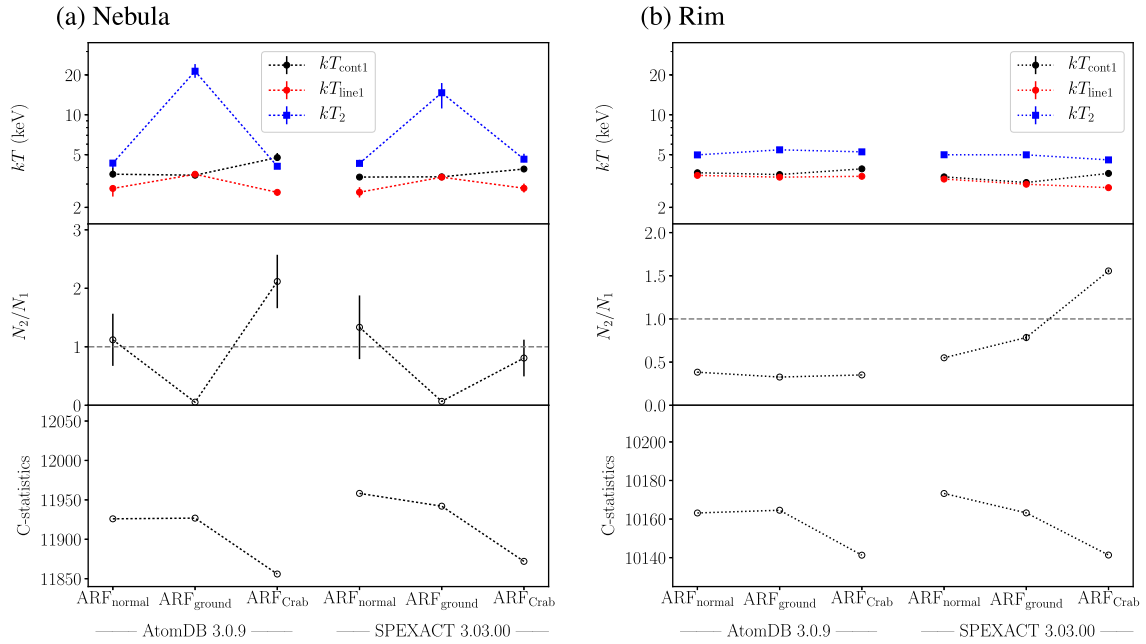
Fig. 18. Fitting results of the 2CIE model with different ARFs in the Nebula and Rim regions. (Color online)

calibration is especially limited. In order to assess the uncertainty of the effective area, two kind of evaluations have been performed, as follows.

The instrument team compared the effective area derived from the ground calibration with that derived from ray-tracing simulations, and found residuals up to ~7% depending on the incident photon energy (figure 15). According to this investigation, the correction factor for the ARF is provided as an `auxtransfile` in CALDB. We corrected the ARF using this database (ARF$_{ground}$).

Tsujimoto et al. (2018) fitted the canonical model ($\Gamma = 2.1$; e.g., Madsen et al. 2015) to the Crab spectrum, and found residuals up to ~10% in the 1.8–20.0 keV band (figure 15). The differences are probably due to uncertainties of not only the telescope reflectivity but also the transmission of the closed gate valve. This calibration method is still not perfect because the spectral extraction region is smaller than that used for the canonical model due to the limited SXS FoV. Nevertheless, we made the local `auxtransfile` according to this result and corrected the ARF (ARF$_{Crab}$).

We made the corrected ARF based on the above corrections factors (ARF$_{ground}$ and ARF$_{Crab}$). As described in sub-subsection 3.2.1, we fitted the spectrum of the Entire Core region with the modified-1CIE model using these corrected ARFs. The residuals in the model with each ARF are shown in figure 16. The best-fit temperatures and normalizations are summarized in figure 7. We also fitted the spectrum with the 2CIE model in the same manner, and show the results in figure 8.

In figures 17 and 18, we show the effect of the different ARFs on the fitting results for the Nebula, Rim, and (where applicable) Outer regions. Similarly in the case of the Entire Core region, the measured values of kT_{line} are consistent with each other, while those of kT_{cont} significantly vary among the ARFs. The 2CIE model in the Nebula region also shows the same tendency as in the Entire Core region, with ARF$_{ground}$ giving an unphysically high temperature of the second component, while the thermal structures inferred for the Rim region are consistent with those for all of the assumed ARFs.

Appendix 5. Line-of-sight velocity dispersion in the 2CIE model

In the 2CIE model described in sub-subsection 3.2.2, the line-of-sight velocity dispersion is $145 \pm 3\,km\,s^{-1}$ and is consistent with the result of the single temperature model in the V paper. In order to investigate the difference in the line-of-sight velocity dispersion between the lower- and higher-temperature components, we untied the link of the parameter between the two plasma models and refit the spectrum. As a result, the velocity dispersions of the lower- and higher-temperature components in `SPEXACT` are $130 \pm 6\,km\,s^{-1}$ and $210^{+47}_{-24}\,km\,s^{-1}$, respectively, whereas those in `AtomDB` are both $145 \pm 7\,km\,s^{-1}$, suggesting that uncertainties of the atomic codes significantly affect the results. Therefore, we found no significant difference in the line-of-sight velocity dispersion between the different temperature components.
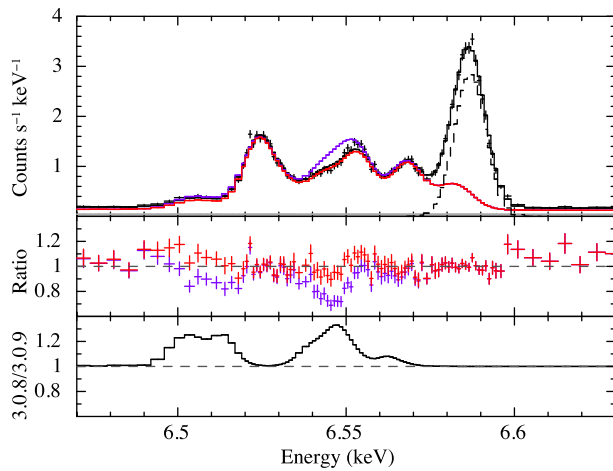
Fig. 19. Comparison between `AtomDB` versions 3.0.9 (red) and 3.0.8 (purple) with the same parameters. The top panel shows the SXS 6.47–6.63 keV spectrum in the Entire Core region with the plasma models. The middle panel is the ratio of the data to the model. The bottom panel shows the ratio of the version 3.0.8 to the version 3.0.9. (Color online)

Table 9. Comparisons of the best-fit parameters between AtomDB version 3.0.9 and 3.0.8.

Model/parameter	AtomDB v3.0.9	AtomDB v3.0.8
Modified-1CIE model		
kT_{cont} (keV)	$4.01^{+0.01}_{-0.01}$	$4.02^{+0.01}_{-0.01}$
kT_{line} (keV)	$3.80^{+0.02}_{-0.02}$	$4.00^{+0.02}_{-0.02}$
N (10^{12} cm^{-5})	$22.77^{+0.04}_{-0.04}$	$23.07^{+0.04}_{-0.04}$
C-statistics/dof	13085.9/12978	13183.5/12978
2CIE model (modified CIE + CIE)		
kT_{cont1} (keV)	$3.66^{+0.01}_{-0.02}$	$4.06^{+0.01}_{-0.01}$
kT_{line1} (keV)	$3.06^{+0.04}_{-0.03}$	$4.03^{+0.03}_{-0.08}$
kT_2 (keV)	$4.51^{+0.02}_{-0.03}$	$1.59^{+0.03}_{-0.17}$
N_1 (10^{12} cm^{-5})	$12.98^{+0.05}_{-0.05}$	$22.64^{+0.05}_{-0.05}$
N_2 (10^{12} cm^{-5})	$9.71^{+0.06}_{-0.05}$	$0.68^{+0.11}_{-0.11}$
C-statistics/dof	13058.5/12976	13178.0/12976

Appendix 6. Comparisons between AtomDB versions 3.0.8 and 3.0.9

In the latest release of `AtomDB` (version 3.0.9), the emissivities of the dielectric-recombination satellite lines for highly charged Fe are changed with respect to version 3.0.8. The difference between versions 3.0.9 and 3.0.8 is shown in figure 19. This difference does not appear to be large, but it significantly affects the result of the 2CIE model as given in table 9. It demonstrates that uncertainties of the atomic code are very significant for the results obtained from high-resolution spectroscopy measurements.

References

Akamatsu, H., & Kawahara, H. 2013, PASJ, 65, 16
Angelini, L., et al. 2017, J. Astron. Telesc. Instrum. Syst., 4, 011207
Arnaud, K. A. 1996, in ASP Conf. Ser., 101, Astronomical Data Analysis Software and Systems V, ed. G. H. Jacoby & J. Barnes (San Francisco: ASP), 17
Arnaud, M., Pratt, G. W., Piffaretti, R., Böhringer, H., Croston, J. H., & Pointecouteau, E. 2010, A&A, 517, A92
Brunetti, G., & Jones, T. W. 2014, Int. J. Mod. Phys. D, 23, 1430007
Bulbul, E., Markevitch, M., Foster, A., Smith, R. K., Loewenstein, M., & Randall, S. W. 2014, ApJ, 789, 13
Cash, W. 1979, ApJ, 228, 939
Churazov, E., Forman, W., Jones, C., & Böhringer, H. 2003, ApJ, 590, 225
Conselice, C. J., Gallagher, J. S., III, & Wyse, R. F. G. 2001, AJ, 122, 2281
de Plaa, J., et al. 2017, A&A, 607, A98
de Plaa, J., Werner, N., Bleeker, J. A. M., Vink, J., Kaastra, J. S., & Méndez, M. 2007, A&A, 465, 345
Eckart, M. E., et al. 2018, J. Astron. Telesc. Inst. Syst., submitted
Fabian, A. C., et al. 2011, MNRAS, 418, 2154
Foster, A. R., Ji, L., Smith, R. K., & Brickhouse, N. S. 2012, ApJ, 756, 128
Fujimoto, R., et al. 2017, J. Astron. Telesc. Instrum. Syst., 4, 011208
Fujita, Y., et al. 2008, PASJ, 60, 1133
Fujita, Y., Kimura, S., & Ohira, Y. 2013, MNRAS, 432, 1434
Fukazawa, Y., Ohashi, T., Fabian, A. C., Canizares, C. R., Ikebe, Y., Makishima, K., Mushotzky, R. F., & Yamashita, K. 1994, PASJ, 46, L55
Gu, L., et al. 2012, ApJ, 749, 186
Gu, L., et al. 2013, ApJ, 767, 157
Hitomi Collaboration 2016, Nature, 535, 117 (First paper)
Hitomi Collaboration 2017a, ApJ, 837, L15
Hitomi Collaboration 2017b, Nature, 551, 478 (Z paper)
Hitomi Collaboration 2018a, PASJ, 70, 9 (V paper)
Hitomi Collaboration 2018b, PASJ, 70, 10 (RS paper)
Hitomi Collaboration 2018c, PASJ, 70, 12 (Atomic paper)
Hitomi Collaboration 2018d, PASJ, 70, 13 (AGN paper)
Inoue, S., Hayashida, K., Ueda, S., Nagino, R., Tsunemi, H., & Koyama, K. 2016, PASJ, 68, S23
Kaastra, J. S. 2017, A&A, 605, A51
Kaastra, J. S., et al. 2004, A&A, 413, 415
Kaastra, J. S., Mewe, R., & Nieuwenhuijzen, H. 1996, in UV and X-ray Spectroscopy of Astrophysical and Laboratory Plasmas, ed. K. Yamashita & T. Watanabe (Tokyo: Universal Academy Press), 411
Kalberla, P. M. W., Burton, W. B., Hartmann, D., Arnal, E. M., Bajaja, E., Morras, R., & Pöppel, W. G. L. 2005, A&A, 440, 775
Kelley, R. L., et al. 2018, J. Astron. Telesc. Instrum. Syst., submitted
Kilbourne, C. A., et al. 2018, PASJ, 70, 18
Leccardi, A., & Molendi, S. 2008, A&A, 486, 359
Madsen, K. K., et al. 2015, ApJ, 801, 66
Makishima, K., et al. 2001, PASJ, 53, 401
Markevitch, M., et al. 2000, ApJ, 541, 542
Markevitch, M., & Vikhlinin, A. 2007, Phys. Rep., 443, 1
Matsushita, K., Belsole, E., Finoguenov, A., & Böhringer, H. 2002, A&A, 386, 77

McNamara, B. R., & Nulsen, P. E. J. 2007, ARA&A, 45, 117

Molendi, S., & Gastaldello, F. 2009, A&A, 493, 13

Nevalainen, J., David, L., & Guainazzi, M. 2010, A&A, 523, A22

Okajima, T., et al. 2016, Proc. SPIE, 9905, 99050Z

Ota, N. 2012, Res. Astron. Astrophys., 12, 973

Peterson, J. R., Kahn, S. M., Paerels, F. B. S., Kaastra, J. S., Tamura, T., Bleeker, J. A. M., Ferrigno, C., & Jernigan, J. G. 2003, ApJ, 590, 207

Pinto, C., et al. 2016, MNRAS, 461, 2077

Planck Collaboration 2013, A&A, 550, A131

Porter, F. S., et al. 2018, J. Astron. Telesc. Instrum. Syst., submitted

Rybicki, G. B., & Lightman, A. P. 1979, Radiative processes in astrophysics (New York: Wiley-Interscience)

Sanders, J. S., & Fabian, A. C. 2007, MNRAS, 381, 1381

Sanders, J. S., Fabian, A. C., & Dunn, R. J. H. 2005, MNRAS, 360, 133

Sanders, J. S., et al. 2016, MNRAS, 457, 82

Sato, T., Matsushita, K., Ota, N., Sato, K., Nakazawa, K., & Sarazin, C. L. 2011, PASJ, 63, S991

Schellenberger, G., Reiprich, T. H., Lovisari, L., Nevalainen, J., & David, L. 2015, A&A, 575, A30

Simionescu, A., et al. 2011, Science, 331, 1576

Simionescu, A., Werner, N., Böhringer, H., Kaastra, J. S., Finoguenov, A., Brüggen, M., & Nulsen, P. E. J. 2009, A&A, 493, 409

Simionescu, A., Werner, N., Mantz, A., Allen, S. W., & Urban, O. 2017, MNRAS, 469, 1476

Takahashi, I., et al. 2009, ApJ, 701, 377

Takahashi, T., et al. 2018, J. Astron. Telesc. Instrum. Syst., submitted

Tsujimoto, M., et al. 2018, PASJ, 70, 20

Vikhlinin, A., Markevitch, M., & Murray, S. S. 2001, ApJ, 551, 160

Wilms, J., Allen, A., & McCray, R. 2000, ApJ, 542, 914